Geochronology, 8, 387–421, 2026
https://doi.org/10.5194/gchron-8-387-2026

Dating circulations of hydrothermal fluids in the crystalline basements of unconformity-related metal deposits using in situ Rb / Sr geochronology: proof of concept

Quentin Boulogne[1,2], Gaétan Milesi[1,2], Chantal Peiffert[1], Emmy Fischer[1,2], Christophe Ballouard[1], Mehdi Serdoun[1,3], Thomas Obin[1,2], Andreï Lecomte[1], Pierre Martz[3], Andrew Kaczowka[4], and Julien Mercadier[1,2]

[1]Université de Lorraine, CNRS, GeoRessources, F-54000 Nancy, France
[2]LabCom CREGU, GeoRessources, CNRS, Université de Lorraine, Vandœuvre-lès-Nancy, France
[3]Orano Canada, Saskatoon, Canada
[4]Cameco Corporation, Saskatoon, Canada

Correspondence: Quentin Boulogne (quentin.boulogne@univ-lorraine.fr)

Received: 24 December 2025 – Discussion started: 20 January 2026
Revised: 5 June 2026 – Accepted: 24 June 2026 – Published: 8 July 2026

Abstract. The use of in situ Rb–Sr geochronology has boomed in recent years following its implementation using LA-ICP-MS/MS technology, which enables fast, in situ analyses at the micron scale on selected minerals. The Rb–Sr geochronometer applied to micas is now commonly used to date the crystallization or cooling of metamorphic and magmatic rocks, based on the assumptions of a closed isotope system after passing the closure temperature and of a homogeneous Sr isotopic composition at the time of crystallization. In situ Rb–Sr geochronology applied to micas and related alteration products in geological contexts involving hydrothermal fluid circulation affecting micas after crystallization could provide a new way to decipher the timing and duration of fluid circulation in various settings such as mountain belts or sedimentary basins. The behavior and applicability of the Rb–Sr system in such contexts are, however, poorly understood, as the system may be partially reopened with differential redistribution of Rb and Sr at the grain scale. To test this hypothesis, we selected a case study related to unconformity-related U deposits from the Athabasca Basin (Canada), which formed through intense hydrothermal fluid circulation at the interface between crystalline basement and siliciclastic sedimentary rocks and represent archetypes of unconformity-related metal deposits. Muscovite grains from metamorphic and magmatic rocks were targeted across a range of alteration states, from hydrothermally unaltered to strongly altered domains. We focused on a specific hydrothermal alteration linked to the formation of hydrothermal illite and sudoite at the expense of metamorphic or magmatic minerals. In unaltered zones, muscovite displays variable but high Rb / Sr ratios, whereas the $^{87}Sr / ^{86}Sr$ intercepts derived from Rb–Sr regressions are scattered and are not interpreted as meaningful initial isotopic compositions. The resulting ages range from ca. 1870 to ca. 1720 Ma and are consistent with the geological context. In distal-to-proximal alteration halos of U deposits, muscovite and related alteration products yield lower $^{87}Rb / ^{86}Sr$ ratios and highly variable regression intercepts. The mean age calculated across the different samples and investigated sites clusters around ∼ 1640 Ma, a value previously obtained by Ar–Ar geochronology on illite and U–Pb geochronology on other hydrothermal phases and proposed to correspond to a major hydrothermal event linked to a geodynamic reorganization affecting the Canadian Shield at the circum-Laurentian scale. The ∼ 1640 Ma age is geologically meaningful in the studied context and is interpreted as reflecting partial, micrometric-scale resetting of the Rb–Sr system in muscovite during this hydrothermal event. The wide range of regression intercept values commonly observed in disturbed Rb–Sr systems is interpreted as an apparent result of open-system behavior, reflecting partial system reopening and non-conservative redistribution of Rb and Sr at the grain scale, rather than as a physically meaningful initial isotopic composition. These results demonstrate that detailed analysis of Rb–Sr system perturbations in al-

tered muscovite and related alteration products can constrain the timing of ancient hydrothermal activity and the spatial dynamics of fluid-rock interaction. This approach provides a valuable complement to conventional fluid-tracing methods and opens new perspectives for reconstructing paleo-hydrothermal systems in ancient basement terrains.

1 Introduction

Crystalline basements are environments in which multiple types of fluids can circulate over geological timescales, depending on the conditions under which these basements formed and later evolved. These fluids may originate from highly diverse sources (magmatic, metamorphic, basin-derived, meteoric, etc.) and display a wide range of physicochemical properties and compositions. Their circulation is primarily driven by first-order geological processes (geodynamic, tectonic, sedimentological, etc.) and is considered to be largely controlled by structural networks, particularly faults, that enhance permeability and enable surface-derived fluids, for instance, to reach depths of several kilometers. Beyond faults and their associated damage zones, fluids may also migrate through broader networks of inherited microfractures and permeable structures within crystalline rocks (e.g., Sibson, 1990; Faulkner et al., 2010; Viswanathan et al., 2022). These fluids can remain stored for millions of years and may be mobilized and/or mixed in response to changes in mechanical conditions (e.g., Anders et al., 2014; Frey et al., 2022). They interact in various ways with the lithologies and mineral assemblages of the basement, inducing mineralogical, chemical, and/or isotopic modifications that may ultimately lead to the formation of various resources such as metal deposits or reservoirs of geothermal waters and metal-rich brines (e.g., Etheridge et al., 1983; Yardley, 1983). Over the past decades, scientific studies have demonstrated, contrary to earlier assumptions, that crystalline basements represent favorable environments for fluid circulation and storage (e.g., Juhász et al., 2002; Walter et al., 2018).

Fluids therefore play a key role in the evolution of crystalline basements, and it is of major scientific importance to identify and date the various episodes of fluid circulation in these environments (e.g., Sibson, 1990; Holness, 2000; Yardley and Bodnar, 2014). Radiometric dating represents a first-order challenge in such contexts, where multiple fluid types may have circulated successively through the same zone in response to large-scale (tectonic) or local-scale (fault-related) geological changes (e.g., Rasmussen et al., 2023; Saito et al., 2018; Weinberg et al., 2020). Each fluid-flow event can leave specific mineralogical markers, often small in size and intermixed with pre-existing minerals. Isotopic dating is also challenging due to the presence of inherited minerals and initial isotopic signatures within the basement, which must be distinguished from those specifically related to each fluid episode (e.g., Dodson, 1973; Grand'Homme et al., 2016). Significant advances have been achieved through the development and application of in situ U–Pb dating of hydrothermal minerals (phosphates, titanium oxides, carbonates, etc.) (e.g., Rasmussen et al., 2001; Rasmussen et al., 2006; Davis et al., 2011; Rabiei et al., 2017; Adlakha and Hattori, 2021). Recent methodological developments in K–Ar dating of clay minerals emphasize the systematic separation of multiple grain-size fractions, combined with detailed mineralogical, crystallographic, and polytype characterization (1Md-1M vs. 2M1 illite), in order to deconvolve mixed detrital and authigenic illite populations and extract meaningful age information related to distinct crystallization or recrystallization events (e.g., Reynolds and Thomson, 1993; Velde and Christophe, 1996; Clauer et al., 1997; Hueck et al., 2022; Gerardin et al., 2024). Such an integrated K–Ar-polytype approach has notably been applied to fault gouges, where dating different clay fractions allows the timing of synkinematic hydrothermal fluid-faulting episodes to be constrained, thereby resolving the temporal evolution of brittle deformation and fluid circulation in fault-controlled hydrothermal systems (e.g., Aldega et al., 2019; Campanha et al., 2025; Schmitz et al., 2025). A limitation of this approach lies in the fact that these minerals are accessory phases, generally present in limited quantities and/or at small spatial scales, which creates difficulties in targeting and identification and often requires the use of costly and time-intensive microscopic techniques, or that they are restricted to specific lithologies or structural contexts.

The development of in situ Rb–Sr geochronology over the past decade has led to a resurgence of interest in the use of micas and feldspars as chronometers in crystalline basements, where they are ubiquitous (e.g., Gyomlai et al., 2023; Jegal et al., 2022; Młynarska et al., 2024; Muñoz-Montecinos et al., 2024). Several studies have demonstrated the relevance of this approach for dating magmatic (e.g., Sundvoll and Larsen, 1990; Tichomirowa et al., 2019; Scott Anderson et al., 2015; Bevan et al., 2021) or metamorphic (e.g., Jenkin et al., 2001; Willigers et al., 2004; Eberlei et al., 2015) events responsible for the crystallization of these minerals, as well as for dating subsequent thermal and/or fluid-related events that affected these primary minerals after their formation, such as in the context of hydrothermal gold deposits (Olierook et al., 2020; Liebmann et al., 2022; Ribeiro et al., 2023a, b; Qiu et al., 2024). These pioneering studies have suggested that the Rb–Sr chronometer may be partially to completely reset within inherited minerals during post-crystallization fluid and/or thermal events. Furthermore, this approach could allow direct dating of hydrothermal circulations affecting basement environments using metamorphic and/or magmatic minerals and their alteration products.

The objective of this contribution is to test this hypothesis in the context of paleo-hydrothermal systems developed at the interface between a crystalline basement and a sedimentary basin. These systems have generated, throughout

Earth history, metal deposits of various commodities such as Pb, Zn, Cu, U, F, and Ba (e.g., Boiron et al., 2010; Cathelineau et al., 2012; Oummouch et al., 2017). The case study focuses on the unconformity-related uranium deposits of the Athabasca Basin (Saskatchewan, Canada), which host the world's highest-grade uranium deposits. These deposits have been the subject of intensive scientific research for over sixty years, and much is known about the typology, age, and geological context of the associated alterations and mineralization. Uranium mineralization formed during hydrothermal episodes that postdated basin deposition and was active in both basin and basement settings. These events led to the formation of localized zones of clay-rich alteration, mainly illite and chlorite, surrounding the orebodies, and are thought to result from interactions between host rocks and evaporitic brines derived from the basin. Although the formation mechanisms are broadly similar to those responsible for other unconformity-related metalliferous deposits worldwide, the interpretation of geochronological data in such long-lived and overprinted hydrothermal systems remains problematic. Existing chronometers commonly yield complex or equivocal age signatures that do not directly correspond to discrete alteration events. This persistent challenge underscores the need to evaluate alternative mineral-isotope system, such as Rb–Sr signatures recorded by basement micas and related hydrothermal products, to more accurately constrain the chronology of alteration associated with the uranium mineralization.

2 Geological settings

2.1 Geological history of the Wollaston-Mudjatik Transition Zone

The Athabasca Basin unconformably overlies the Archean to Paleoproterozoic basement rocks known as the Western Churchill Structural Province (WSP). The WSP is divided into two lithostructural subprovinces: the Rae Subprovince to the west and the Hearne Subprovince to the east (Annesley et al., 2005) (Fig. 1A). The Trans-Hudson Orogeny (THO), which represents a major Paleoproterozoic belt, is linked to the collision between the Rae, Hearne, and Superior cratons. The beginning of this orogeny is characterized by the amalgamation between 1920 and 1840 Ma of the Rae and Hearne cratons, leading to the formation of the Western Churchill Structural Province (WSP) and to an oceanic arc in the Manikewan Ocean (Ansdell, 2005; Corrigan, 2012; Corrigan et al., 2005, 2009). The gradual closure of the Manikewan Ocean led to the successive accretion of juvenile crustal segments between 1880 and 1860 Ma. The final stage of the THO resulted in the complete closure of the Manikewan Ocean and in the continental collision between the margin of the Hearne craton bordered by the accreted juvenile arcs and the northern edge of the Superior craton between 1830 and 1800 Ma (Corrigan et al., 2009). Finally, the latter stages of THO deformation are marked by the emplacement at ca. 1800 and 1720 Ma of pegmatites and aplites, in relation to sinistral deformation along shear bands in a transpressional context (e.g., Chiarenzelli, 1989; Bickford et al., 1990; Chiarenzelli et al., 1998; Bickford et al., 2005; Schneider et al., 2007).

The western margin of the Hearne Craton comprises two distinct domains of Paleoproterozoic age: the Mudjatik domain and the Wollaston domain (Fig. 1A). The Mudjatik domain is predominantly composed of Archean tonalite-trondhjemite felsic gneiss domes (2640–2580 Ma; Annesley et al., 1997a, b, 1999a, b). In contrast, the Wollaston domain is composed mainly of Paleoproterozoic metasediments attributed to the Wollaston Supergroup (deposited at ca. 2050–1860 Ma; Yeo and Delaney, 2007; Tran et al., 2008), including paragneisses, banded iron formations, quartzites, and marbles. These units are interpreted as evidence of sedimentation initially controlled by a passive-margin setting, which evolved into a back-arc basin and then into a foreland basin in response to tectonic processes related to the collision phase (Annesley et al., 2005; Jeanneret et al., 2016). The two lithotectonic domains are separated by the Wollaston-Mudjatik Transition Zone (WMTZ), within which the present study area is located (Fig. 1A). This zone exhibits an anastomosed structure oriented from northeastern to southwestern, a trait that was inherited from the THO. The deformation phases associated with the various stages of THO formation mentioned above can be observed within this zone.

The basement rocks underwent three tectonometamorphic events. The first event (M1–D1) is dated from ca. 1840 to 1813 Ma based on U–Pb dating of monazite and zircon from migmatitic metapelites of the Wollaston Supergroup. These rocks host a garnet-cordierite ± sillimanite assemblage that experienced partial melting at peak conditions of 750–825 °C and $\leq$ 1 GPa (Annesley et al., 1992, 1997a, b, c, 1999a, b; Jeanneret et al., 2017; Toma et al., 2024). The second event (M2–D2), dated from ca. 1813 to 1770 Ma, is recorded within migmatites and pegmatites. It corresponds to an isothermal decompression down to 0.5–0.9 GPa at temperatures of 750–825 °C, within the stability field of cordierite under suprasolidus conditions, as constrained by U–Pb dating of monazite and zircon (Annesley et al., 1992, 1997a, b, c, 1999a, b; Jeanneret et al., 2017; Toma et al., 2024). The third event corresponds to an exhumation and orogenic cooling phase. Although its onset is poorly constrained, this phase is generally considered to extend from ca. 1770 Ma (750 °C, 0.5 GPa) to ca. 1720 Ma (350 °C, 0.2 GPa), as documented by several studies (Annesley and Madore, 1994; Annesley et al., 1992, 1997a, b, c, 2005; Jeanneret et al., 2017; Martz, 2017). This exhumation phase is characterized by pronounced retrograde transformations linked to early-stage hydrothermal activity. These include the breakdown of cordierite in favour of phyllosilicates, biotite chloritization, remobilization and precipitation of sulfides, graphite, and muscovite, circulation of quartz-rich

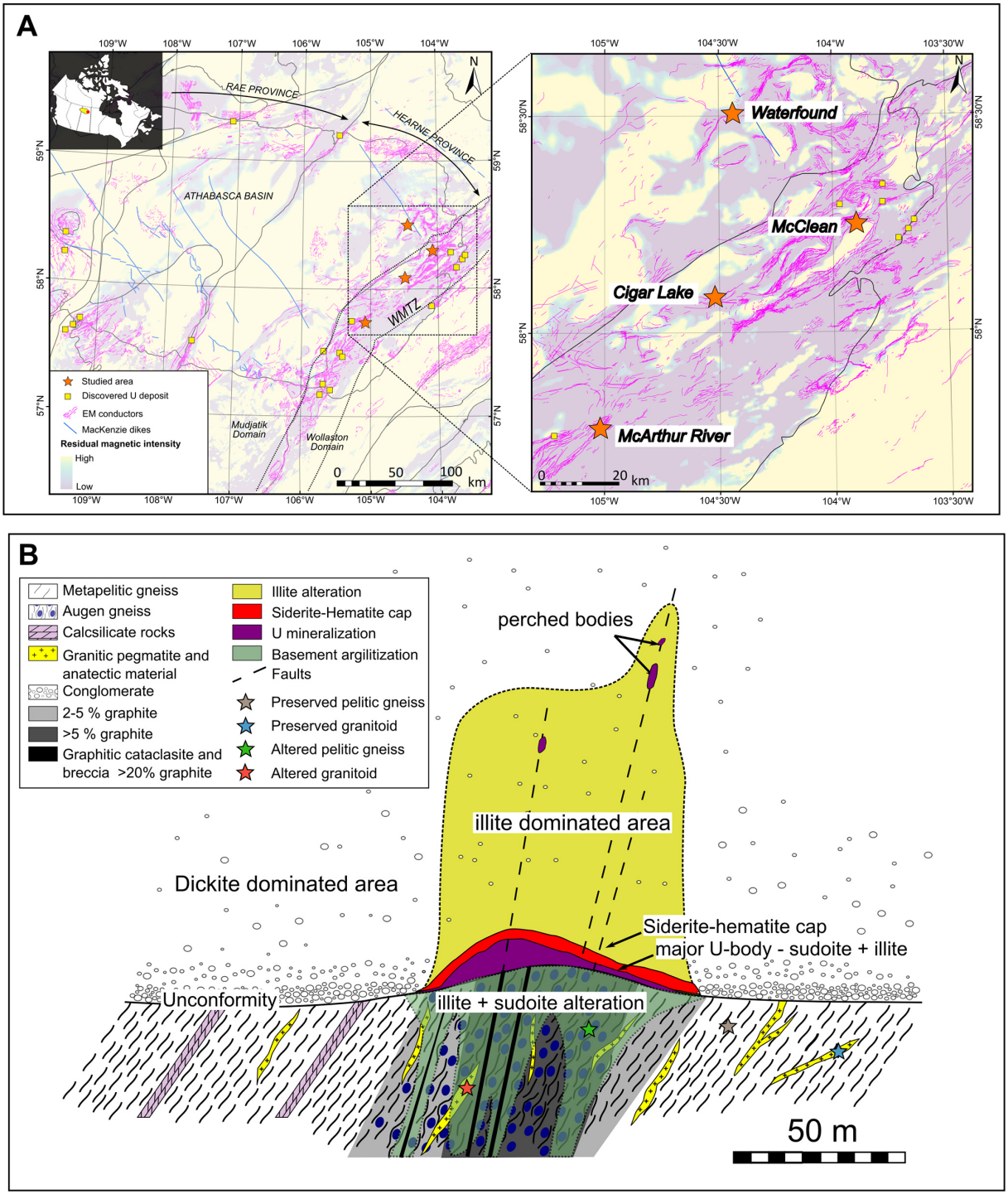

Figure 1. **(A)** Left: map of the Athabasca Basin (Saskatchewan, Canada) with the outline of the different lithotectonic units forming the basement. Right: zoom of the study area located in the eastern part of the Athabasca Basin along the WMTZ. The graphitic conductors (in magenta) are interpreted from electromagnetic (EM) data by the Saskatchewan Geological Survey (SGS) from airborne EM surveys, and correspond to graphitic-rich shear zones hosting uranium mineralization. The yellow squares represent deposits or mineralizations with economic potential, and the blue stars represent the studied sites. Data source: Saskatchewan Geological Survey (electromagnetic data). Map created using ArcGIS Pro. Coordinate Reference System (CRS): WGS 84. **(B)** Schematic cross-section through the main ore body of Cigar Lake, archetype of unconformity-related U deposits. U is located at the unconformity above a ductile-brittle graphitic shear zone (modified after Martz et al., 2019a) and is associated with an alteration halo dominated by illite and sudoite in both basin and basement. The theoretical locations of the four types of samples examined in this study are indicated by colored stars.

fluids, and dissolution-reprecipitation processes affecting monazite and zircon (Card, 2012, 2014; Card and Noll, 2016).This phase is further constrained by cooling ages derived from biotite Rb–Sr (Worden et al., 1985; Schneider et al., 2007), muscovite K–Ar (Philippe et al., 1993), and muscovite Ar–Ar systems (Alexandre et al., 2009).

2.2 Geological history of the Athabasca Basin

The Paleoproterozoic to Mesoproterozoic Athabasca Basin is a large intracratonic basin located in northern Saskatchewan and Alberta (Ramaekers et al., 2007). The sedimentary sequence of this basin, known as the Athabasca Supergroup, was deposited between ca. 1760–1720 Ma (Ramaekers et al., 2007; Jeanneret et al., 2016) and 1541 Ma for the youngest known age (Creaser and Stasiuk, 2007). Stratigraphic, geochronological, and fluid-inclusion $P-T$ data indicate that the basin reached a maximum depth of 2 to 5 km depending on the methods considered (Pagel et al., 1975a, b; Chi et al., 2018), with a preserved thickness of 1.5 km today (Hobson et al., 1969). The stratigraphic sequence is organized into four major clastic sedimentary sequences that record a progressive deepening of the basin (Jefferson et al., 2007). The first sequence, represented by the Fair Point Formation, consists of conglomerates and quartz-pebble arenites infilling the Jackfish Sub-basin, located in the western part of the basin, during the initial sag phase around 1760 Ma (e.g., Ramaekers et al., 2007; Pehrsson et al., 2023). The second sequence, including the Smart/Read and Manitou Falls formations, fills the Cree Sub-basin, situated in the eastern and southeastern parts of the basin, and reflects the development of a shallow half-graben with NW-directed palaeoflow between 1680 and 1650 Ma (Ramaekers et al., 2007; Jeanneret et al., 2016; Pehrsson et al., 2023). The third sequence, represented by the Lazenby Lake and Wolverine Point formations, shows vertical fining and records a major paleoenvironmental shift around 1640 Ma, characterized by abrupt deepening in the western basin, a marine incursion, and a transition to axial palaeocurrents sourced from the north or east (Rainbird et al., 2007; Ramaekers et al., 2007), as indicated by vitric tuff layers dated at 1644 ± 13 Ma (U–Pb zircon; Rainbird et al., 2007). The final sequence, which includes the Locker Lake, Otherside, Douglas, and Carswell formations, reflects detrital and marine sedimentation during continued subsidence and tectonic reorganization associated with the Kuungmi rifting (Pehrsson et al., 2023), notably recorded by organic-rich black shales of the Douglas Formation dated by Re–Os at 1541 ± 13 Ma (Creaser and Stasiuk, 2007). Overall, the basin maintains a largely coherent oval geometry with minimal deformation, except for the Ordovician Carswell impact structure, which locally disrupts the Athabasca Supergroup (Ramaekers et al., 2007; Pehrsson et al., 2023).

2.3 Petrographic and metallogenic characteristics of unconformity-related uranium deposits in the Athabasca Basin

The Athabasca Basin unconformity-related uranium deposits are globally renowned for their exceptionally high grades, reaching up to 20 wt % U_3O_8. The principal uranium deposits are concentrated in the eastern part of the Athabasca Basin and are spatially associated with a NE-SW-trending anastomosed transition zone inherited from the Trans-Hudsonian Orogeny (THO), commonly referred to as the Wollaston-Mudjatik Transition Zone. This structural corridor comprises a ca. 50-km-wide network of graphite-rich shear zones, typically described as graphite conductors, as they exhibit high electrical conductivity, a physical property that allows their detection by electromagnetic geophysical methods used for uranium exploration (Fig. 1). The uranium deposits are spatially associated with graphite-rich shear zones, and uranium orebodies show diverse morphologies and structural associations depending on their location: (i) at the unconformity, within the first meters of sandstones and conglomerates; (ii) within the basement, extending several hundred meters below the unconformity along shear zones; or (iii) as perched deposits located tens to hundreds of meters above the unconformity within the sedimentary sequence. The mineralized zones are surrounded by hydrothermal alteration halos that can extend several tens of meters into both the basin and the basement and serve as critical geochemical and mineralogical guides for U exploration. In the basin, alteration halos overlying basement-hosted deposits or surrounding sandstone-hosted mineralization are dominated by illite, with variable amounts of kaolinite, sudoite (tri-dioctahedral Mg-chlorite), and dravite (magnesian tourmaline), depending on the deposit.

Within the basement, three principal alteration types are superimposed, as exemplified by the world-class Cigar Lake deposit (Fig. 1B). The first type corresponds to retrograde metasomatic alteration related to the final exhumation and orogenic cooling phase of the Trans-Hudsonian Orogeny (THO). It is marked by partial to complete biotite chloritization, discrete quartz and muscovite crystallization, and hydrothermal graphite formation. These alteration types and their associated petrographic features have been extensively documented in the vicinity of unconformity-related uranium deposits within the Athabasca Basin (e.g., Carl et al., 1992; Derome et al., 2005; Cloutier et al., 2011; Mercadier et al., 2011; Alexandre et al., 2012; Adlakha and Hattori, 2015; Martz et al., 2019a; Menier et al., 2020; Powell et al., 2022). The second type corresponds to regolithic alteration developed within the upper tens of meters of the basement following its exhumation after the Trans-Hudsonian Orogeny. It is characterized by a laterally correlative weathering profile comprising four zones: (i) a bleached kaolinite-rich and hematite-depleted zone at the unconformity; (ii) a highly oxidized hematite-rich zone; (iii) a red-green transitional zone

characterized by hematite and chlorite; and (iv) a thicker green-to-red zone enriched in illite, chlorite, and hematite (e.g., Macdonald, 1980; Halter, 1988). The third type corresponds to post-basin-deposition hydrothermal alteration, which represents the most extensive alteration type. It is proposed to be linked with uranium mineralization and is characterized by the massive replacement of primary minerals by an illite- and sudoite-dominated clay assemblage.

The main accepted model for the formation of these deposits is known as "diagenetic-hydrothermal" and involves the circulation of oxidized brines of marine origin containing NaCl-$CaCl_2$ at temperatures of around 120–200 °C in the basin and underlying bedrock (Derome et al., 2005; Richard et al., 2011, 2013, 2015). The interaction of these brines with basin and/or basement rocks favors the formation of alteration halos and mobilizes uranium in its oxidized form (U^{6+}), which is transported through fractures and reactivated graphitic structures. Uranium precipitates within structural and physicochemical traps, where dissolved hexavalent uranium (U^{6+}) is reduced to tetravalent uranium (U^{4+}) (Hoeve and Sibbald, 1978; Jefferson et al., 2007).

Published absolute ages for the precipitation of primary uranium mineralization at the scale of the basin span a broad range, from ca. 1590 to 1200 Ma. These estimates derive from U–Pb analyses of UO_2 and from K–Ar or Ar–Ar geochronology of clay minerals (Cumming and Krstic, 1992; Philippe et al., 1993; McGill et al., 1993; Fayek and Riciputi, 2002; Alexandre et al., 2009; Cloutier et al., 2011; Powell et al., 2022). Building on these age constraints, an alternative hypothesis invoking an earlier episode of uranium mineralization and/or hydrothermal alteration merits consideration. Numerous studies have shown that U–Pb systematics of uraninite and associated alteration minerals in unconformity-related deposits are commonly overprinted by multiple fluid-flow events, resulting in partial Pb loss and a broad dispersion of apparent ages (Kotzer and Kyser, 1990; Fayek and Kyser, 1997; Fayek et al., 2002; Fayek and Riciputi, 2002; Kyser et al., 2015). Consequently, the existence of an older hydrothermal system, potentially active in the ca. 1640–1680 Ma interval, cannot be ruled out and may be cryptic due to subsequent alteration, uranium remobilization, and isotopic resetting during younger tectono-hydrothermal episodes. This interpretation is consistent with evidence for repeated basin-scale fluid circulation and late-stage meteoric fluid ingress documented in the Athabasca Basin, processes that are known to modify both clay mineral K–Ar / Ar–Ar ages and uraninite U–Pb signatures. A similarly complex temporal evolution is recognized in unconformity-related uranium systems of northern Australia, where in situ U–Pb analyses of uraninite suggest initial mineralization or hydrothermal alteration as early as ca. 1680–1640 Ma, followed by multiple younger resetting events extending into the Mesoproterozoic and Paleozoic (Clauer et al., 2015; Skirrow et al., 2016).

3 Materials and methods

3.1 Sampling strategy

Four study areas located in the northeastern segment of the Wollaston-Mudjatik Transition Zone (WMTZ) were selected to evaluate the applicability of in-situ Rb–Sr geochronology to date the main hydrothermal alteration (illite-sudoite) associated with the U mineralisation within the basement rocks. From north to south, these areas comprise the Waterfound (WF) and McClean South (MCS) prospects, and the Cigar Lake (CL) and McArthur River (MAC) deposits. All samples from WF, MCS, and CL analyzed in this study were obtained from drill cores collected during the past five years as part of U exploration programs conducted by Orano Canada Inc., whereas samples from MAC were provided by Cameco Corporation. The sampling strategy at the four study sites was designed to ensure both lateral and vertical representativeness, spanning from unaltered basement zones (Fig. 2A, B) to hydrothermally altered domains characterized by illite-sudoite assemblages associated with the mineralization (Fig. 2C, D, E, F). For MCS, five drill holes were considered from west to east: MCS-03, MCS-05, MCS-34, MCS-35C and MCS-31 (mineralized conductor). For WF, six drill holes were considered from southwest to northeast: WF-93, WF-98, WF-66, WF-77 and WF-75 (mineralized conductor) and WF-100 (outside the La Rocque Conductive Corridor). For CL, two drill holes were considered from west to east: WC-449 (mineralized conductor) and WC-473 (non-mineralized conductor). For MAC, five drill holes were considered from west to east: MC-408, MC-408-01, MC-418, MC-410-01, MC-410-02 (mineralized conductor). Pelitic gneisses and anatectic granitoids represent the two dominant lithologies within the WMTZ, particularly within the graphite-rich shear zones that host mineralization, which justifies their selection for this study. Across all investigated sites, four samples of pelitic gneisses unaffected by illite-sudoite alteration were analyzed, together with five samples of anatectic granitoids and/or associated leucosomes that were likewise preserved from this alteration. Their altered equivalents comprise ten samples of pelitic gneisses affected by illite-sudoite alteration and nineteen samples of anatectic granitoids and/or leucosomes exhibiting the same alteration signature. All samples were specifically selected based on their high muscovite modal abundances and the presence of muscovite grains of sufficient size to enable in situ Rb–Sr analyses by LA-ICP-MS.

3.2 Methods

Scanning electron microscopy (SEM), electron probe microanalysis (EPMA), and micro-X-ray fluorescence (µ-XRF) analyses were performed at the Service Commun de Microscopies Électronique et de Microanalyse X (SCMEM) in Nancy, France, whereas in situ Rb–Sr isotopic analyses were

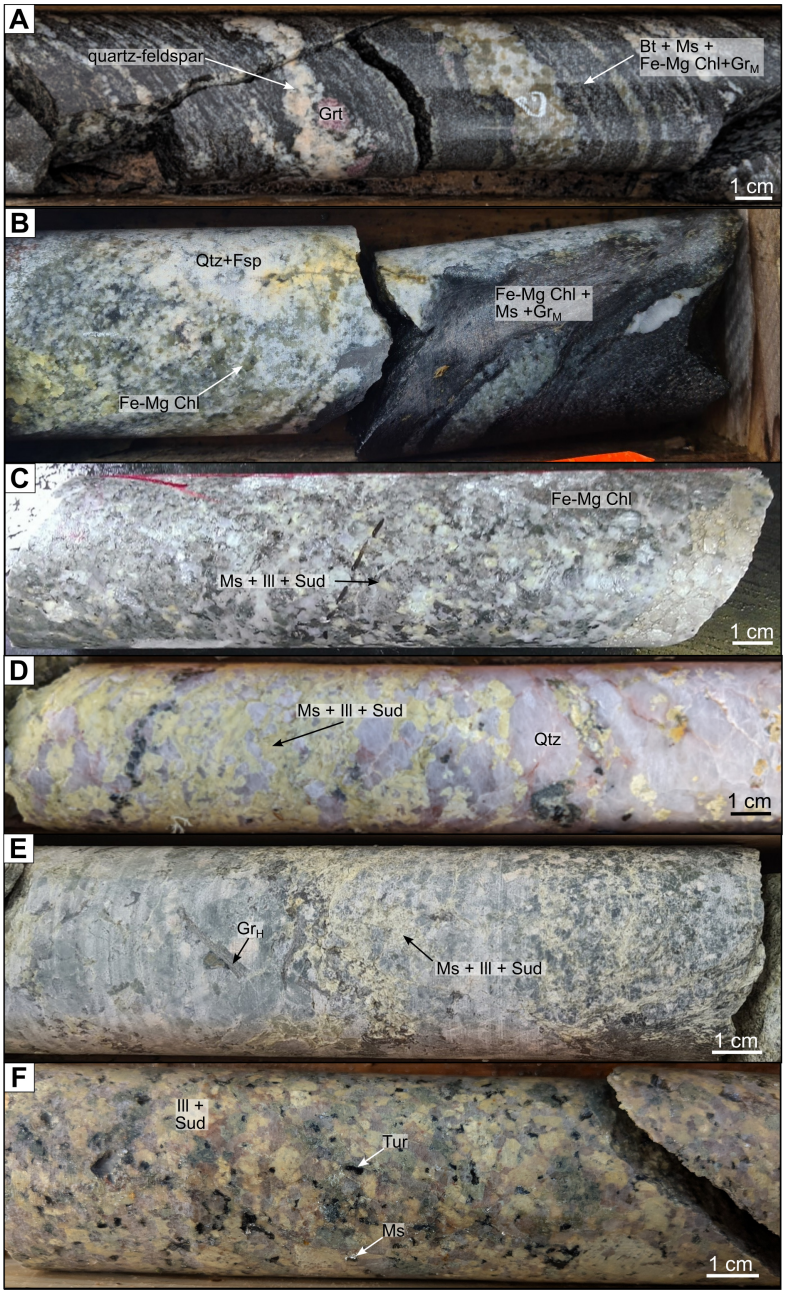

Figure 2. Macroscopic pictures of drill cores intervals sampled for this study **(A)** Anatectic pelitic gneiss containing metamorphic graphite (Gr_M), biotite (Bt), muscovite (Ms) and Fe-Mg chlorite (Fe-Mg Chl) within the restite; the contact between the quartz-feldspar leucosome (Qtz+Fsp) and the restite is marked by garnet. Evidence of retro-metamorphic alteration is visible within the quartz-feldspar leucosome and is characterized by a fir-green coloration [MC-408_591.3 m]. **(B)** Anatectic pelitic gneiss showing an accumulation of metamorphic graphite in the restite; the quartz-feldspar leucosome exhibits retro-metamorphic alteration features, with Fe-Mg chlorite imparting a dark green coloration to the core rock [MCS-05_285.5 m]. The restite is composed of metamorphic graphite, biotite, muscovite. **(C)** Strongly altered granitoid characterized by nearly complete replacement of feldspars and plagioclase by illite and sudoite (Ill+Sud), while quartz and ferromagnesian chlorites remain preserved. Here, muscovite is embedded within the illite-sudoite assemblage and is not macroscopically observable [WC-449_434.4 m]. **(D)** Granitoid exhibiting pervasive illite-sudoite alteration, within which muscovite is entirely incorporated into the fine-grained alteration matrix and is not discernible at the macroscopic scale [MC-410-02_687.4 m]. **(E)** Anatectic pelitic gneiss hosting hydrothermal graphite (Gr_H) concentrations within the leucosome, associated with the retrograde metamorphic features and an illite-sudoite alteration matrix in which muscovite is cryptic and not macroscopically distinguishable. [MCS-34_273.7 m]. **(F)** Granitoid exhibiting intense illite-sudoite alteration of primary minerals, imparting an apple-green coloration to the entire drill core, with muscovite and tourmaline (Tur) also locally preserved and macroscopically visible [WF-93_581.0 m].

carried out on the ICP platform at GeoRessources, Université de Lorraine (Nancy, France).

3.2.1 Petrography – Optical and SEM

Samples were first observed using a conventional optical microscope under transmitted light. Thin-section scale mapping was conducted using a Keyence VHX-2000 optical macroscope. Muscovite and associated minerals were imaged using a TESCAN VEGA 3 LM scanning electron microscope (SEM). This SEM is equipped with a conventional tungsten filament and is coupled to two Bruker XFlash 6–30 mm^2 EDS detectors. The backscattered electron (BSE) images were obtained using the following parameters: an accelerating voltage of 15 kV, a working distance (WD) of 15 mm, a beam current of 0.5 nA, and an acquisition speed of 1 ms per pixel.

3.2.2 X-ray fluorescence (XRF)

Thin sections were analyzed using a BRUKER M4 TORNADO micro-XRF, which enables localized analysis of elements ranging from sodium to uranium, with a maximum spatial resolution of approximately 20 µm and a sensitivity varying from around one percent for light elements (Na) to several tens of ppm for more sensitive elements (Zr). The device is equipped with a rhodium X-ray tube, polycapillary optics to focus the beam and two Bruker SDD-type EDS detectors to enhance acquisition speed, allow for the identification of diffraction peaks, and reduce shadowing effects. Mapping parameters included a 35 µm step size, with a dwell time of 10 ms, corresponding to a scan speed of 3.5 mm s^{-1}. X-ray tube parameters were set to 400 µA and 50 kV, under a 2 Pa vacuum. µ-XRF data were subsequently processed using the M4 TORNADO software to generate elemental maps.

3.2.3 Electron probe microanalysis (EPMA)

X-ray elemental maps of K (Kα), Rb (Kα), Mg (Kα), Al (Kα), Ca (Kα), F (Kα), Fe (Kα), Mn (Kα) and Na (Kα) on selected areas in thin sections were carried out using a CAMECA SX5 TACTIS electron microprobe, equipped with a LaB6 tip and five vertical WDS spectrometers. The analytical conditions included a beam current of 100 nA, an accelerating voltage of 25 kV, and a counting time of 20 ms per pixel.

3.2.4 In situ Rb–Sr isotopic analysis (LA-ICP-MS/MS)

In situ Rb–Sr analyses on muscovite were carried out using a LA-ICP-MS/MS system. The $^{87}Rb/^{86}Sr$ and $^{87}Sr/^{86}Sr$ ratios of the studied samples and reference materials were determined using an Agilent 8900 ICP-MS/MS coupled with a 193 nm ArF excimer laser ablation system ESI 193 nm ArF with a TwoVol2 dual-volume ablation cell. All samples were ablated employing a 50 µm spot size for 90 to 110 s (30 to 40 s of gas blank measurement and 30 to 40 s of ablation time followed by 30 s of sample washout), with a repetition rate of 10 Hz and a laser energy density of 6 J.cm^{-2}. Helium at a flow rate of 700 mL min^{-1} was used as a carrier gas in the ablation cell, then mixed with N_2 via a Y connector at a flow rate of 4 mL min^{-1} and argon nebulization gas at a flow rate of 700 mL min^{-1} before entering the ICP-MS torch. The reaction gas N_2O was used to overcome isobaric interferences to separate ^{87}Sr from ^{87}Rb due to the efficiency of N_2O in reacting with Sr^+ to form SrO^+ ions, which was not the case for Rb^+. The following isotopes were measured (integration time in parentheses): $^{28}Si \rightarrow {}^{28}Si$ (2 ms), $^{84}Sr \rightarrow {}^{84}Sr$ (5 ms), $^{84}Sr \rightarrow {}^{100}SrO$ (120 ms), $^{85}Rb \rightarrow {}^{85}Rb$ (20 ms), $^{85}Rb \rightarrow {}^{101}Rb$ (5 ms), $^{86}Sr \rightarrow {}^{86}Sr$ (5 ms), $^{86}Sr \rightarrow {}^{102}SrO$ (120 ms), $^{87}Sr \rightarrow {}^{87}Sr$ (5 ms), $^{87}Sr \rightarrow {}^{103}SrO$ (120 ms), $^{88}Sr \rightarrow {}^{88}Sr$ (5 ms), $^{88}Sr \rightarrow {}^{104}SrO$ (120 ms). A scan of all isotopes (sampling period) took approximately 565 ms. Seven sessions were conducted to analyze all samples. The NIST SRM 610 glass (Woodhead and Hergt, 2001) and MicaMg mica (Hogmalm et al., 2017, Jegal et al., 2022) were used as external standards for the correction of the $^{87}Sr/^{86}Sr$ and $^{87}Rb/^{86}Sr$ ratios, respectively. Although matrix effects between phlogopite and natural muscovite cannot be entirely excluded when using MicaMg as primary reference material for $^{87}Rb/^{86}Sr$ correction (Glorie et al., 2024), its use currently remains unavoidable as it represents the only widely available and internationally distributed nano-powder reference material specifically designed and validated for in situ Rb–Sr dating by LA-ICP-MS/MS. La Posta biotite was used as a secondary reference material to monitor the stability of the instrumental setup and the long-term reproducibility of the analytical protocol. It has a reported weighted mean age of 93.8 ± 2.5 Ma and an initial $^{87}Sr/^{86}Sr$ ratio of 0.70483 ± 0.0005 (ID-TIMS, Walawender et al., 1990). The Sr/Sr_i value for La Posta calculated using NIST 610 is consistent and further confirmed by the value calculated for MicaMg via NIST 610. Reproducing both the reference age and the initial Sr isotopic composition provides an independent assessment of analytical accuracy. To quantitatively evaluate long-term reproducibility, La Posta analyses acquired over a three-year period were grouped by analytical session. For each session, an isochron age was calculated independently. The resulting session ages were then combined using a weighted mean, in which each session age was weighted by the inverse square of its internal uncertainty, and the dispersion of individual session ages around this weighted mean, quantified as the standard deviation of the weighted residuals, yields an external reproducibility of approximately 1.6 % (2σ), which is adopted as a realistic estimate of long-term analytical uncertainty (Supplement Fig. S1). Final age uncertainties reported in this study incorporate both the internal analytical uncertainty and this external reproducibility through quadrature propagation, such that $\sigma\_\text{total} = \sqrt{(\sigma\_\text{internal}^2 + \sigma\_\text{reproducibility}^2)}$. The overall weighted mean age is 93.9 ± 1.2 Ma (2σ) with an MSWD

of 0.38. In addition, regression intercepts from individual sessions were compiled to calculate a weighted mean initial $^{87}Sr/^{86}Sr$ ratio of 0.7045 ± 0.0018 (2σ). This value is in excellent agreement with the ID-TIMS constrained value of 0.70483 reported by Walawender et al. (1990). The consistency of both age and intercept values over three years demonstrates robust long-term stability of Sr isotopic measurements. These results indicate no evidence for significant instrumental drift, calibration bias, or matrix-dependent effects, and effectively exclude an analytical origin for the anomalously low initial $^{87}Sr/^{86}Sr$ values observed in some samples. LA-ICP-MS/MS data reduction was performed using Iolite 4 (Paton et al., 2011). The processed and calibrated data for $^{87}Sr/^{86}Sr$ and $^{87}Rb/^{86}Sr$ ratios were plotted in conventional isochron and radial plots and used to calculate Rb–Sr isochron ages and corresponding regression intercepts using IsoplotR (Vermeesch, 2018). In the following, regression intercepts refer strictly to the mathematical intercepts of Rb–Sr regressions and are not interpreted as true initial $^{87}Sr/^{86}Sr$ ratios.

Concentrations of ^{87}Rb, ^{86}Sr, and ^{87}Sr were calculated from LA-ICP-MS isotopic measurements using a reproducible procedure that accounts for isotopic abundances, measured Rb–Sr ratios, and matrix effects. Total ^{87}Rb concentrations (ppm) were derived from the measured ^{85}Rb signal by correcting for the natural isotopic abundances ($^{85}Rb = 0.7217$, $^{87}Rb = 0.2783$) of Rb according to Eq. (1):

$$^{87}Rb = {}^{85}Rb_{measured} \times \frac{0.2783}{0.7217} \quad (1)$$

Concentrations of ^{86}Sr were then calculated from the measured $^{87}Rb/^{86}Sr$ ratios obtained from the Rb–Sr regression diagrams according to Eq. (2):

$$^{86}Sr = \frac{^{87}Rb}{\left(^{87}Rb/^{86}Sr\right)_{measured}} \quad (2)$$

Subsequently, ^{87}Sr concentrations were calculated using the measured $^{87}Sr/^{86}Sr$ ratios according to Eq. (3):

$$^{87}Sr = \left(^{87}Sr/^{86}Sr\right)_{measured} \times {}^{86}Sr \quad (3)$$

To correct for instrumental fractionation and sample–standard differences, a matrix correction factor of 0.532038 was applied to all calculated concentrations according to Eq. (4):

$$C_{corrected} = C_{calculated} \times 0.532038 \quad (4)$$

This factor was determined from the internal standard MicaMg by comparing the measured ^{85}Rb concentration with its published reference value (Jegal et al., 2022) and then applied proportionally to ^{87}Rb, ^{87}Sr, and ^{86}Sr in all samples. The complete dataset of raw Rb–Sr isotope ratios, single-spot ages, uncertainties, and matrix-corrected elemental concentrations is provided in Supplement Table S1.

4 Results

Two types of muscovite, identified in the least altered zones of the metasomatic halos, are investigated (Fig. 2A and B): (i) (retro-)metamorphic muscovite associated with the retrograde mineral assemblage within metamorphic rocks and (ii) early hydrothermal muscovite within magmatic rocks as a secondary phase. All of the studied samples exhibit evidence of a first alteration associated with the retrograde metamorphism and are variably overprinted by a second hydrothermal alteration that is described below.

4.1 Metamorphic muscovite

Metamorphic muscovite is exclusively developed along the foliation planes of Paleoproterozoic metapelites (Fig. 2A, B) (e.g., Schneider et al., 2007; Skipton et al., 2016; Jeanneret et al., 2017; Martz, 2017). These rocks are characterized by quartz and sericitized K-feldspar, and are bounded by graphite-rich shear zones containing biotite, muscovite, and pyrite (Fig. 3A). Biotite occurs as lath-shaped crystals, locally plastically deformed showing *C*-*S* planes, ranging from 0.5 to 1 mm in length, and oriented parallel to the subvertical S1 foliation. Muscovite is present as euhedral to subhedral crystals, predominantly crystallizing along the rims of metamorphic biotite, with an orientation perpendicular to the S1 foliation, suggesting a crystallization stage postdating biotite growth possibly along the retrograde $P-T$ path (Fig. 3A). Muscovite is also present within pressure shadows around biotite mica-fish, suggesting that muscovite crystallization was contemporaneous with ductile deformation (Fig. 3B). Metamorphic biotites are locally pseudomorphosed by Fe-Mg chlorite, a marker of retrograde metamorphism or fluid-induced alteration (Fig. 3C). The metamorphic muscovite is commonly associated with medium-sized, euhedral to tabular flakes of metamorphic graphite aligned along the foliation. Sulfides such as pyrite and chalcopyrite are frequently associated with this metamorphic graphite (Fig. 3D).

4.2 Early hydrothermal muscovite

Early hydrothermal muscovite occurs within anatectic granitoids or within the leucosomes of metapelitic gneisses (Fig. 2C, D, E, F) (e.g., Schneider et al., 2007; Skipton et al., 2016; Martz, 2017; Obin, 2025). These lithologies are primarily composed of quartz, K-feldspar of the microcline type, often altered to sericite forming very fine microlamellar aggregates with a shimmering whitish-grey appearance, plagioclase, and biotite laths, which are partially to completely pseudomorphosed by Fe-Mg chlorite (Fig. 3E, F). Muscovite in these rocks occurs either as subhedral crystals or as fibrous aggregates that may have partially to completely replaced chloritized biotite or have precipitated along biotite grain boundaries as fine-grained crystals (Fig. 3E, F, G). It may also have locally replaced K-feldspar (Fig. 3F). Mus-

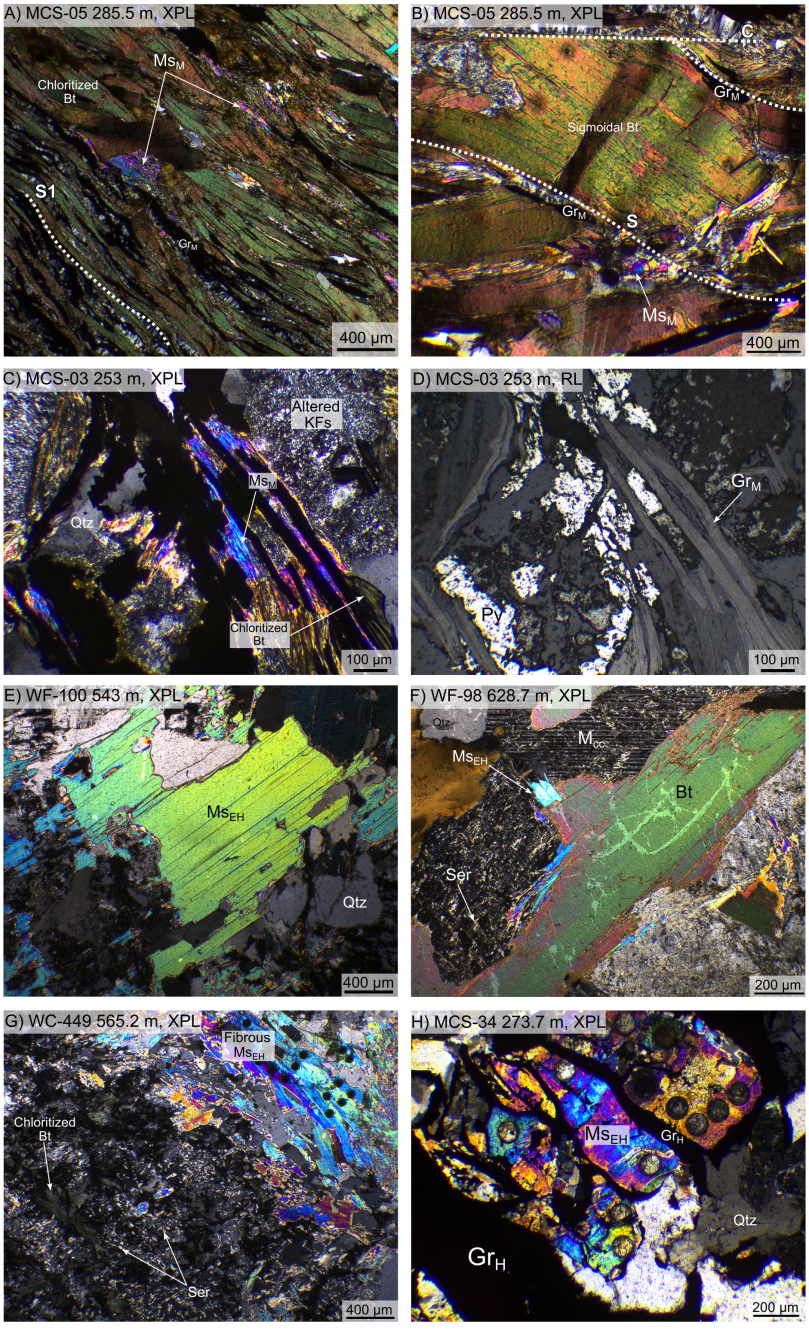

Figure 3. **(A–B)** Graphitic pelitic gneiss [MCS-05_285.5 m]. **(A)** Pelitic gneiss displaying a well-developed foliation. Biotite (Bt) and thick flakes of metamorphic graphite (Gr_M) are aligned along the S1 foliation, while retrograde metamorphic muscovite (Ms_M) crystallizes at the rims of biotite, perpendicular to S1. **(B)** Plastically deformed biotite marking a C-S fabric, with fine-grained metamorphic muscovite precipitating around biotite and within biotite pressure shadows. **(C–D)** Graphitic pelitic gneiss with retrograde mineral assemblage [MCS-03_253 m]. Assemblage of quartz (Qtz), K-feldspar (KFs), metamorphic muscovite, pyrite (Py), and metamorphic graphite, that has undergone chloritization related to retrograde metamorphic alteration. Metamorphic muscovite is aligned with tabular flakes of metamorphic graphite. **(E–F)** Granitoid rocks. **(E)** Subhedral early hydrothermal muscovite (Ms_{EH}) crystals [WF-100_543 m]. **(F)** Assemblage of biotite, quartz, and microcline (M_{cc}), showing early stages of sericitization (Ser). Early hydrothermal muscovite precipitated as a secondary phase along biotite grain boundaries and has locally replaced, now altered and sericitized, K-feldspar [WF-98_628.7 m]. **(G)** Leucosome of metapelitic gneiss characterized by fibrous aggregates of early hydrothermal muscovite crosscutting partially to completely chloritized biotite [WC-449_565.2 m]. **(H)** Leucosome of metapelitic gneiss with early hydrothermal muscovite associated with large flakes of hydrothermal graphite (Gr_H) [MCS-34_273.7 m].

covite is frequently associated with hydrothermal graphite, which occurs as large flakes (up to 0.5 cm) precipitating interlayered with muscovite within late fractures or forming radiating patterns in granitic leucosomes (Fig. 3H). These lithologies may also be locally enriched in tourmaline, occurring as euhedral to subhedral crystals with strong relief and second-order yellow to green interference colors. Accessory phases include zircon, monazite, and apatite, present as subhedral crystals or as veinlets crosscutting the aforementioned minerals.

4.3 Petrographic characteristics of altered muscovites

This hydrothermal alteration affects both metamorphic muscovite (Fig. 4A–C) and early hydrothermal muscovite (Fig. 4D–I). This Mg-K-type alteration pervasively affects the two lithologies that constitute the graphite-rich shear zones, whether through the mylonitic foliation planes of pelitic gneisses (Fig. 4A–C), the grain boundaries of magmatic to early hydrothermal minerals in anatectic granitoids and leucosomes (Fig. 4D–I), or through fracture networks indiscriminately crosscutting the two lithologies. At the microscopic scale, this alteration is expressed by the extensive replacement of primary and retro-metamorphic minerals by a clay assemblage predominantly composed of micrometric illite, spatially associated with sudoite (a magnesium-rich trioctahedral chlorite). However, this alteration is not uniformly distributed within the different lithologies, and the illite/sudoite ratio varies between lithologies and within the same lithology (Fig. 4D, G). In anatectic granitoids and leucosomes, the alteration is marked by the partial replacement of K-feldspar and the complete replacement of plagioclase, which are more prone to alteration, by this clay assemblage (Fig. 4D–I). Fractures crosscutting quartz and feldspars are commonly filled with illite and/or sudoite crystals (Fig. 4A). The cleavage planes of muscovite are partially to completely disrupted, and their birefringence colors approach those of illite, reflecting the onset of muscovite illitization, particularly visible along grain margins (Fig. 4E, F, H, I). Under cross-polarized light, illite occurs as lath-shaped crystals (Fig. 4E, F, H, I). Sudoite appears as needle-like crystals with low relief, generally $< 2\,\mu m$ in length (Fig. 4B, C, H, I). Figure 5 highlights the effect of illite-sudoite alteration within a single sample (MC-410-01, 677.9 m), comparing a relatively preserved zone showing the onset of alteration (Fig. 5A) with a fully altered zone (Fig. 5B). Backscattered electron (BSE) images reveal that in the least altered area, muscovite retains its characteristic cleavage planes (Fig. 5A), whereas in the most altered area, muscovite has completely lost its original morphology and is replaced by sudoite ± illite. Mixtures of these two phases can be distinguished through grayscale contrast variations (Fig. 5B). Elemental X-ray maps obtained by EPMA further emphasize these mineralogical and chemical transformations (Fig. 5C–H). In the least altered zone, muscovite exhibits variable K (Kα) intensities, with maximum values in the most preserved domains and progressively decreasing intensities in areas showing incipient alteration (Fig. 5C). The Rb (Kα) signal follows a similar pattern, reaching its highest values in the K-rich zones (Fig. 5E). This decrease in K and Rb intensities correlates with the occurrence of Mg (Kα)-rich areas associated with sudoite formation along fracture zones (Fig. 5G). In the most altered zone, muscovite relics (or "ghosts") are identified by their relatively high K (Kα) and Rb (Kα) intensities (Fig. 5D, F), which are spatially anti-correlated with the Mg (Kα) signal. The latter reaches its maximum intensity within the sudoite matrix that surrounds these muscovite remnants (Fig. 5H).

4.4 In situ Rb–Sr geochronology

Rb–Sr isotopic analyses were performed on metamorphic and early hydrothermal muscovite sampled from both unaltered and illite-sudoite-altered zones, and from the two investigated lithologies (Table S1). To assess the impact of the illite-sudoite alteration on the isotope system of basement minerals, a representative sample of a pelitic gneiss (MC-410-01, at a depth of 677.9 m) containing both well-preserved (Fig. 6A, B) and partially preserved to altered muscovite grains (Fig. 6C, D) was selected for detailed in situ analysis by LA-ICP-MS/MS. The complete Rb–Sr dataset obtained from this sample defines a Rb–Sr regression corresponding to a date of 1761.9 ± 30.6 Ma ($n = 34$, MSWD $= 5.8$, $p \approx 0$, 2σ internal; ± 41.6 Ma including external reproducibility), with $^{87}Rb / ^{86}Sr$ ratios ranging from 19.62 to 670.44 and a corresponding $^{87}Sr / ^{86}Sr$ intercept of 0.6524 ± 0.0096 (Fig. 6E). The elevated MSWD value and the null probability associated with the reduced χ^2 test indicate significant excess scatter in the isotopic data, consistent with heterogeneous isotopic behavior at the grain scale. Given this dispersion, Rb–Sr single-spot dates were calculated for each laser ablation point following the approach of Rösel and Zack (2022), allowing for a direct comparison between isotopic data, petrographic observations, and elemental mapping. The resulting single-spot dates display a systematic relationship with K (Kα) intensity maps, showing a decrease in apparent dates with decreasing K intensity, consistent with the progressive alteration of muscovite (Fig. 6B, D). Radial plots illustrating the distribution of single-spot dates and isotope ratios (Galbraith, 1988, 1990; Rösel and Zack, 2022) reveal two statistically distinguishable populations with partial overlap: a dominant population at 1785.2 ± 11.2 Ma (76.8 %), corresponding predominantly to the least altered muscovite domains, and a younger population at 1646.9 ± 20.4 Ma (23.2 %), associated with increasingly altered domains (Fig. 6F). When plotted separately on Rb–Sr regression diagrams, analyses from the least altered muscovite domains yield a statistically robust regression corresponding to a date of 1789.1 ± 37 Ma ($n = 23$, MSWD $= 0.51$, $p = 0.9689$, 2σ internal; ± 47 Ma including external reproducibility), with a $^{87}Sr / ^{86}Sr$ in-

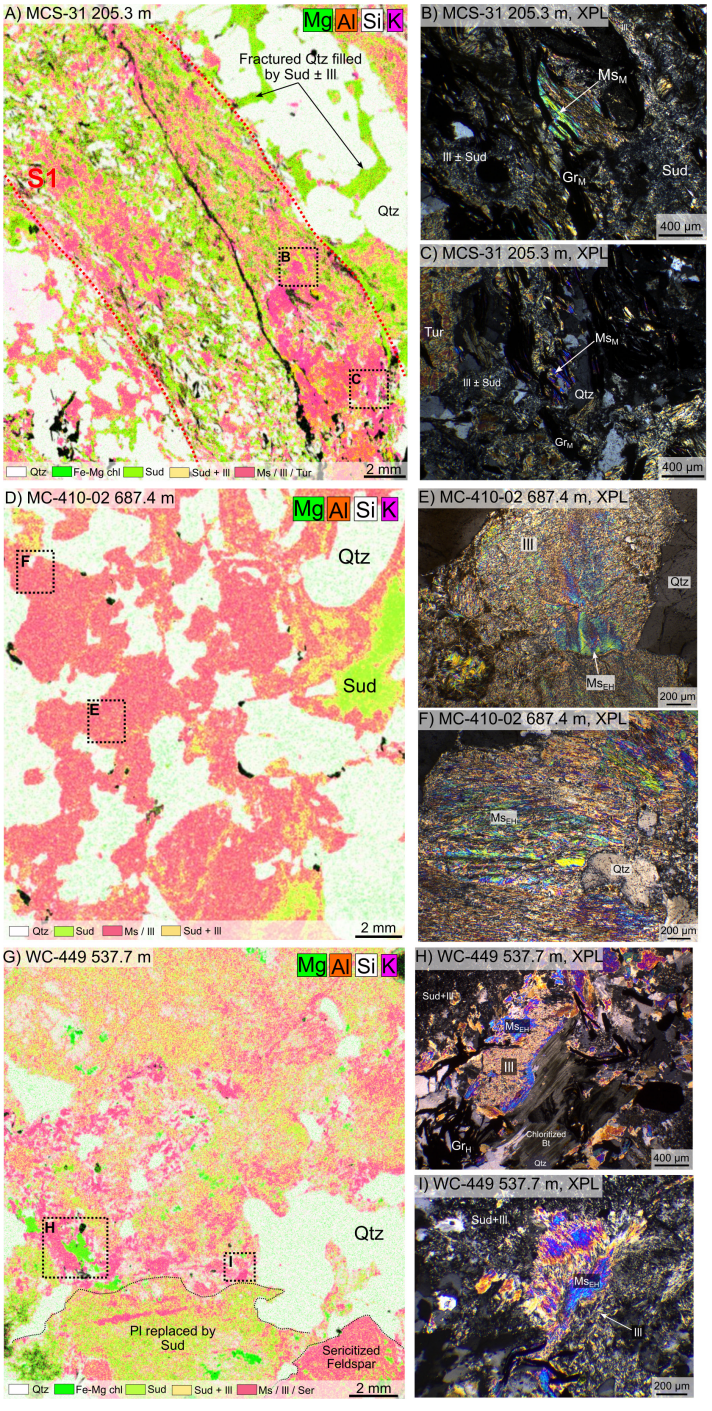

Figure 4. **(A)** Micro-X-ray fluorescence (µ-XRF) elemental maps of a thin section showing the distribution of Mg, Al, Si, and K within a migmatitic graphitic pelitic gneiss including a leucosome [MCS-31_205.3 m]. Illite (Ill)-sudoite (Sud) alteration is hosted along the mylonitic foliation planes of pelitic gneisses and occurs pervasively within the leucosome. Sudoite also precipitates within fractures crosscutting the quartz (Qtz) vein. **(B–C)** Magnified views of **(A)** showing illite-sudoite alteration affecting metamorphic muscovite (Ms_M). **(D)** µ-XRF elemental mapping displaying the Mg, Al, Si, and K distribution within an anatectic granitoid [MC-410-02_687.4 m]. Illite/sudoite ratios vary across the sample, with domains that are fully illitized and others enriched in sudoite. **(E–F)** Magnified views of **(D)** illustrating the illitization of early hydrothermal muscovite (Ms_{EH}). **(G)** µ-XRF elemental maps showing the Mg, Al, Si, and K distribution within an anatectic granitoid [WC-449_537.7 m]. Illite and sudoite crystallize pervasively, with spatial variations in the illite/sudoite ratio. **(H–I)** Magnified views of **(G)** showing early hydrothermal muscovite illitization and the coexistence of illite-sudoite replacing early minerals. Biotite associated with early hydrothermal muscovite is completely chloritized.

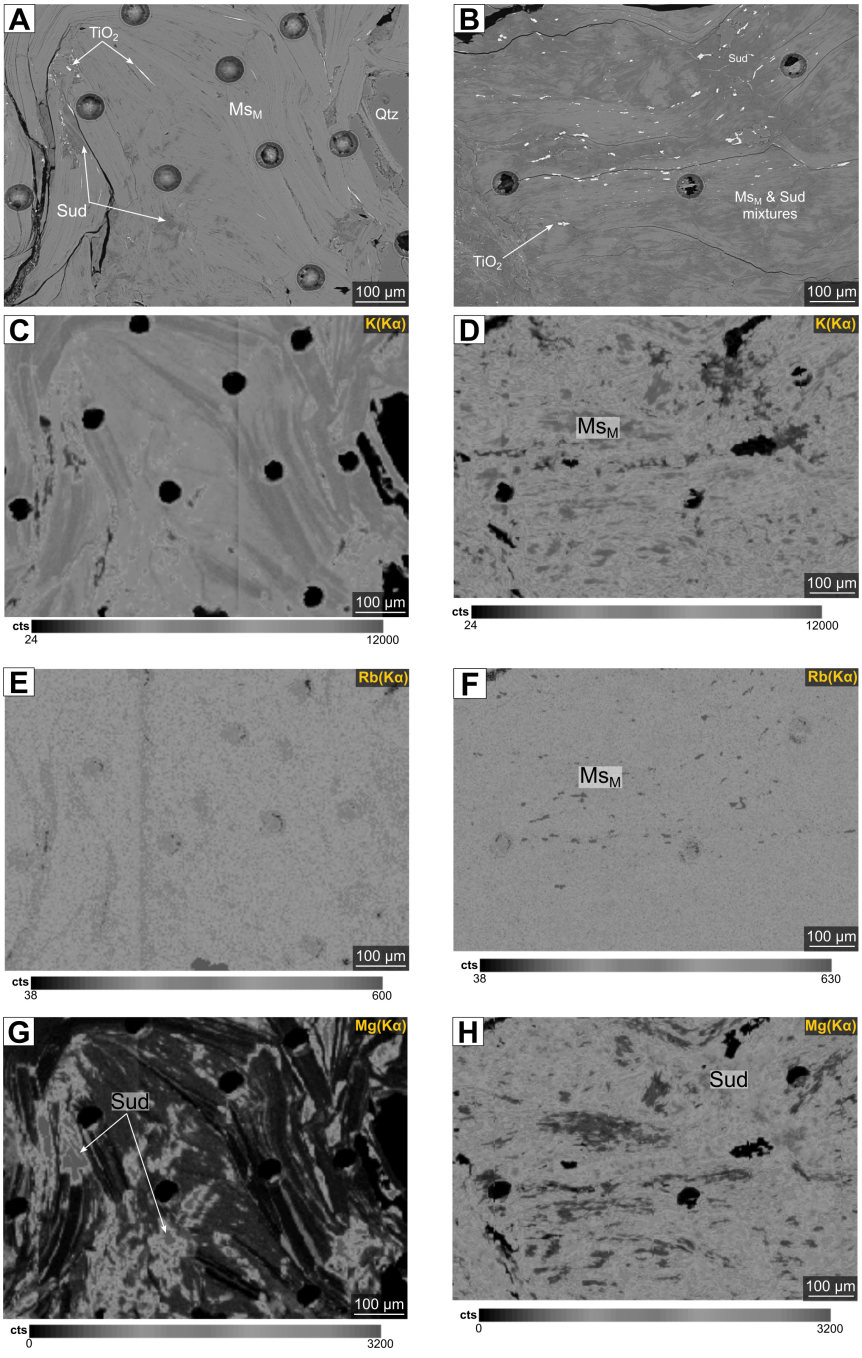

Figure 5. Two zones within the same pelitic gneiss sample [MC-410-01, 677.9 m] are shown, ranging from weakly altered **(A, C, E, G)** to strongly altered by sudoite **(B, D, F, H)**. **(A)** Preserved to partially preserved metamorphic muscovite (Ms_M) showing the onset of alteration to sudoite along fractures, expressed by darker grey tones. **(B)** Strongly altered metamorphic muscovite replaced by a sudoite-dominated matrix, containing very fine (< 1 µm) TiO_2 exsolution lamellae that formed from the alteration of muscovite. Circular holes correspond to 50 µm-diameter laser ablation pits. **(C–D)** X-ray elemental maps of K (Kα) for **(A)** and **(B)**, respectively. **(C)** Gradual decrease in apparent K concentration from the fully preserved zone toward the incipiently altered domain. **(D)** K-enriched "ghosts" of muscovite, whereas altered zones are strongly to entirely depleted in K. **(E–F)** X-ray elemental maps of Rb (Kα) acquired by EPMA for **(A)** and **(B)**, respectively. Apparent Rb concentration is higher in the most preserved zones in **(E)** and within muscovite ghosts in **(D)** compared with illite-sudoite zones. **(G–H)** X-ray elemental maps of Mg (Kα) acquired by EPMA for **(A)** and **(B)**, respectively. **(G)** Zones filled with sudoite are highlighted by high apparent Mg concentrations. **(H)** Apparent Mg concentration is maximal in sudoite-rich areas and anticorrelated with the K distribution shown in **(D)**.

tercept of 0.6709 ± 0.0115 (Fig. 6G). In contrast, analyses from the more altered and mixed domains define a less statistically reliable regression at 1659.5 ± 55.4 Ma ($n = 11$, MSWD $= 4.1$, $p = 2.6 \times 10^{-5}$, internal; ± 61 Ma including external reproducibility), associated with a $^{87}Sr / ^{86}Sr$ intercept of 0.6316 ± 0.018 (Fig. 6H). The elevated MSWD values obtained for the altered domains again indicate substantial isotopic scatter. On the basis of these observations and the coexistence of mixed isotopic populations within a single sample, the analytical approach applied to the entire dataset, supported by petrographic and microstructural evidence, consisted of distinguishing the most preserved metamorphic and early hydrothermal muscovite from those more strongly altered by an illite-sudoite clay assemblage, in order to constrain the crystallization dates of these two muscovite types and the potential timing(s) of alteration (Fig. 7A–E).

4.5 Rb–Sr dating of metamorphic muscovite

The weighted mean of the Rb–Sr data obtained from all preserved metamorphic muscovite grains (four samples) defines a composite Rb–Sr regression at 1780.8 ± 14.6 Ma ($n = 57$, MSWD $= 0.92$, $p = 0.63$, 2σ internal; ± 32 Ma including external reproducibility), associated with a $^{87}Sr / ^{86}Sr$ intercept of 0.6704 ± 0.0075 and overall $^{87}Rb / ^{86}Sr$ ratios ranging from 19 to 671 (Fig. 7A). Rb–Sr single-spot dates for preserved metamorphic muscovite were calculated using a fixed $^{87}Sr / ^{86}Sr$ reference value of 0.6704, corresponding to the intercept of the composite regression. This value is used here as an operational reference parameter; owing to its low magnitude, reasonable variations in this parameter exert only a minor influence on the calculated dates, as previously demonstrated by Rösel and Zack (2022). The resulting single-spot dates range from 1760 ± 30 to 1914 ± 88 Ma and define a single statistically coherent population with a modal value of 1771.2 Ma (Fig. 7E). Matrix-corrected elemental concentrations (using an applied correction factor of 0.532038) range from 33 to 145 ppm (average: 81 ppm) for ^{87}Rb, from 0.19 to 2.46 ppm (average: 1.03 ppm) for ^{86}Sr, and from 1.28 to 4.50 ppm (average: 2.73 ppm) for ^{87}Sr.

4.5.1 Rb–Sr dating of early hydrothermal muscovite

The weighted mean of the Rb–Sr data obtained from preserved early hydrothermal muscovite (five samples) defines a composite regression at 1753.4 ± 12.4 Ma ($n = 53$, MSWD $= 0.87$, $p = 0.73$, 2σ internal; ± 31 Ma including external reproducibility), associated with a $^{87}Sr / ^{86}Sr$ intercept of 0.6989 ± 0.0168 and overall $^{87}Rb / ^{86}Sr$ ratios ranging from 34 to 514 (Fig. 7B). Rb–Sr single-spot dates for preserved early hydrothermal muscovite were calculated using the same fixed $^{87}Sr / ^{86}Sr$ reference value of 0.6704, which has a negligible influence on the resulting dates (e.g., Rösel and Zack, 2022). The calculated single-spot dates span from 1701.9 ± 57.6 to 1799.5 ± 42.8 Ma and cluster into a single statistically consistent population with a modal value of 1752.1 Ma (Fig. 7E). Matrix-corrected elemental concentrations (using an applied correction factor of 0.532038) range from 60.5 to 144.7 ppm (average: 111.3 ppm) for ^{87}Rb, from 0.22 to 2.26 ppm (average: 0.55 ppm) for ^{86}Sr, and from 1.82 to 3.97 ppm (average: 3.15 ppm) for ^{87}Sr.

4.5.2 Rb–Sr dating of altered muscovites

The weighted mean of the dates obtained for the metamorphic muscovite affected by illite-sudoite hydrothermal alteration defines regressions at ca. 1635 Ma for metamorphic muscovite (ten samples, $n = 224$, MSWD $= 8.8$, $p = 0$, 2σ internal; ± 26 Ma including external reproducibility) and at ca. 1636 Ma for early hydrothermal muscovite (nineteen samples, $n = 733$, MSWD $= 6.2$, $p = 0$, 2σ internal; ± 26 Ma including external reproducibility), associated with $^{87}Sr / ^{86}Sr$ intercepts of 0.6976 ± 0.0029 and 0.7091 ± 0.0055, respectively (Fig. 7C, D). The elevated MSWD values and null probabilities indicate significant excess scatter in both datasets for both muscovite types. Single-spot Rb–Sr dates obtained from altered muscovite display a broad and erratic distribution, ranging from 1498.6 ± 22.8 to 1756.2 ± 45.8 Ma (modal value of 1637.2 Ma) for metamorphic muscovite, and from 1357.0 ± 64.8 to 1735.1 ± 43.8 Ma (modal value of 1645.6 Ma) for early hydrothermal muscovite (Fig. 7E). Matrix-effect-corrected concentrations for the metamorphic muscovite range from 21.7 to 213.6 ppm (mean: 99.9 ppm) for ^{87}Rb, from 0.10 to 3.74 ppm (mean: 0.62 ppm) for ^{86}Sr, and from 0.9 to 5.8 ppm (mean: 2.76 ppm) for ^{87}Sr. Matrix-effect-corrected concentrations for the early hydrothermal muscovite range from 9.18 to 3222.9 ppm (mean: 190.4 ppm) for ^{87}Rb, from 0.05 to 15.8 ppm (mean: 0.82 ppm) for ^{86}Sr, and from 0.44 to 75.4 ppm (mean: 4.95 ppm) for ^{87}Sr.

The analysis of calculated single-spot Rb–Sr dates as a function of uncertainty quartiles reveals an overall homogeneous distribution, with moderate variations in central values and dispersion across uncertainty levels (Fig. 8A). The dataset was divided into four groups corresponding to the uncertainty quartiles (Q0–Q25, Q25–Q50, Q50–Q75, and Q75–Q100). The group with the lowest uncertainty (Q0–Q25) comprises 241 observations, yielding a mean date of 1633.3 Ma ($\sigma = 45.3$ Ma). The second quartile (Q25–Q50) includes 239 samples, with a mean date of 1630.7 Ma ($\sigma = 44$ Ma). In the third quartile (Q50–Q75), the mean remains stable at 1630.6 Ma, although the standard deviation increases slightly ($\sigma = 51.5$ Ma), reflecting greater variability. Finally, the quartile with the highest uncertainty (Q75–Q100) encompasses 239 data points, showing a slightly higher mean date (1637.2 Ma) and the greatest dispersion ($\sigma = 53.9$ Ma). Examination of the minimum and maximum values indicates a gradual broadening of the single-spot Rb–Sr date distribution with increasing uncertainty, ranging from 1493.8 to 1752.7 Ma in the first quartile to 1357.0 to

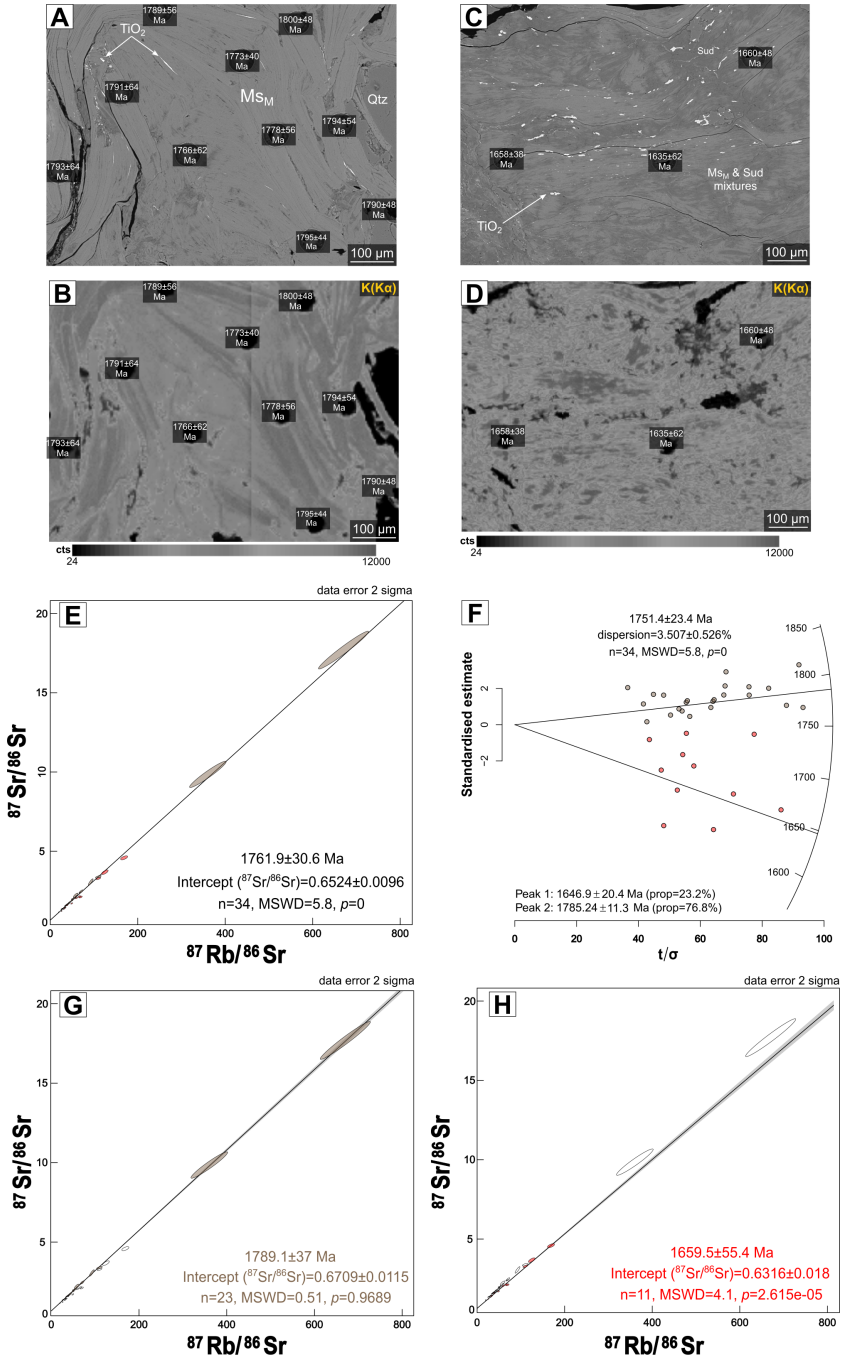

Figure 6. **(A–D)** BSE images and corresponding X-ray elemental maps of K (Kα) acquired by EPMA for the pelitic gneiss sample [MC-410-01, 677.9 m] shown in Fig. 5, displaying the calculated Rb–Sr single-spot dates (Rösel and Zack, 2022) for each ablation pit. **(A–B)** The calculated Rb–Sr single-spot dates decrease toward zones exhibiting reduced apparent K concentrations. **(C–D)** The calculated Rb–Sr single-spot dates are significantly younger in domains fully altered to sudoite compared to those in **(A)** and **(B)**, which correspond to preserved to partially preserved zones. **(E)** Muscovite Rb–Sr isochrons for the sample [MC-410-01, 677.9 m] obtained from both preserved and altered areas. **(F)** Radial plot showing the dispersion of isotope ratios and calculated single-spot dates in preserved and altered domains (Galbraith, 1988, 1990; Rösel and Zack, 2022), revealing two main populations. **(G)** Muscovite Rb–Sr isochrons for preserved domains of the sample [MC-410-01, 677.9 m]. **(H)** Muscovite Rb–Sr isochrons for altered domains of the same sample. Brown symbols correspond to preserved muscovite, and red symbols correspond to partially to completely altered muscovite. All errors are reported at 2σ.

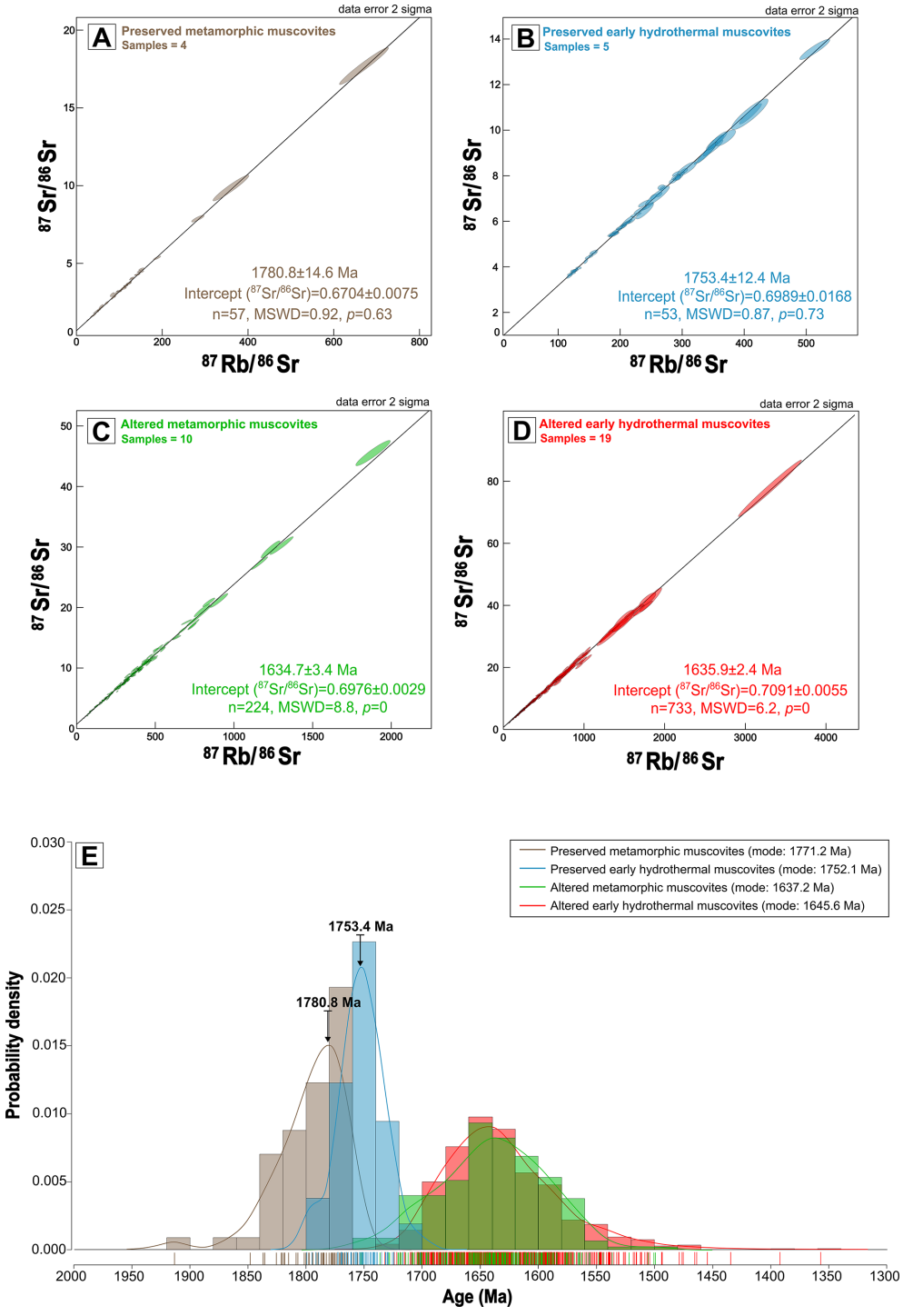

Figure 7. **(A)** Rb–Sr isochrons for metamorphic muscovite preserved from illite-sudoite alteration, represented by four samples. **(B)** Rb–Sr isochrons for early hydrothermal muscovite preserved from illite-sudoite alteration, represented by five samples. **(C)** Rb–Sr isochrons for metamorphic muscovite affected by illite-sudoite alteration, represented by ten samples. **(D)** Rb–Sr isochrons for early hydrothermal muscovite affected by illite-sudoite alteration, represented by nineteen samples. **(E)** Density diagram constructed from individual single-spot dates obtained for preserved metamorphic muscovite (brown), preserved early hydrothermal muscovite (blue), illite-sudoite altered metamorphic muscovite (dark red), and illite-sudoite altered early hydrothermal muscovite (red). A bin width of 20 Ma was used for the histogram. The isochron dates calculated in **(A)** and **(B)** are indicated by bold arrows for the preserved metamorphic and early hydrothermal muscovite.

1751.5 Ma in the last. This trend suggests that measurements associated with higher uncertainties encompass a wider range of dates (Fig. 8B). Overall, the kernel density estimates (KDE) of single-spot date distributions by quartile display relatively similar patterns, indicating no major bias related to analytical uncertainty, although a slight increase in variability is observed. This observation highlights that, while individual uncertainties do not significantly affect the mean of the single-spot dates, they are associated with greater dispersion in the extreme values. To address the heterogeneous distribution of single-spot dates and the variability of their individual uncertainties, a statistical approach based on a Gaussian Mixture Model (GMM) was applied (McLachlan and Peel, 2000; Melnykov and Melnykov, 2012; Glodek et al., 2013; Nguyen and McLachlan, 2015; McLachlan et al., 2019). The GMM, applied to the logarithmically transformed Rb–Sr single-spot dates of both muscovite types, enables the decomposition of the overall dataset into multiple components characterized by distinct probabilistic centers. A suite of GMMs with varying numbers of Gaussian components was evaluated, with model performance assessed using the Bayesian Information Criterion (BIC), which balances goodness of fit against model complexity. Although solutions with different numbers of components were obtained, the five-component model emerged most consistently across repeated runs and is therefore presented here. This configuration is compatible with the number of populations identified from IsoplotR radial plots (Galbraith, 1988, 1990), providing a coherent basis for methodological comparison. The GMM-derived components were subsequently examined in relation to the statistically coherent clusters defined by the radial plot approach, which explicitly accounts for individual analytical uncertainties. Statistical analyses conducted on the hydrothermally altered muscovite show good overall consistency between the date clusters identified by the radial plots (IsoplotR) and those inferred from the GMM. For altered metamorphic muscovite, the radial plot reveals five statistical groupings (Fig. 8C): 1517.6 ± 6.2 Ma (1.8 % of analyses), 1587.4 ± 3.0 Ma (24.7 %), 1629.5 ± 3.2 Ma (31.7 %), 1662.5 ± 3.2 Ma (25.4 %), and 1709.5 ± 3.4 Ma (16.4 %). The corresponding GMM also distinguishes multiple components, including a dominant one at 1650.0 ± 28.8 Ma (33.3 %), and secondary components at 1698.8 ± 40.4 Ma (18.9 %), 1623.1 ± 27.2 Ma (24.5 %), 1585.5 ± 36.0 Ma (21.0 %), and 1519.6 ± 44.4 Ma (2.4 %) (Fig. 8D). For altered early hydrothermal muscovite, the radial plot identifies five statistical clusters (Fig. 8E): 1466.3 ± 6.4 Ma (1.7 % of analyses), 1542.5 ± 3.0 Ma (8.1 %), 1597.9 ± 2.2 Ma (23.5 %), 1642.3 ± 1.6 Ma (41 %), and 1684.0 ± 1.6 Ma (25.8 %). The corresponding GMM also resolves several components, including a main one at 1640.4 ± 32.4 Ma (38.4 %), and secondary components at 1680.0 ± 37.4 Ma (31.7 %), 1597.2 ± 36.4 Ma (19.7 %), 1545.9 ± 38.6 Ma (8.1 %), and 1480.8 ± 91.4 Ma (1.8 %) (Fig. 8F). When combining the results for illite-sudoite zones of both muscovite types, the radial plot identifies five statistical clusters (Fig. 8G): 1493.0 ± 4.4 Ma (2.7 % of analyses), 1562.9 ± 3.2 Ma (11.2 %), 1609.3 ± 2.8 Ma (27.4 %), 1649.0 ± 2.2 Ma (37.6 %), and 1691.4 ± 2.0 Ma (21.1 %). The corresponding GMM also distinguishes several components, including a dominant one at 1641 ± 32.8 Ma (37.6 %), and secondary components at 1681.1 ± 42.4 Ma (28.2 %), 1599.2 ± 35.2 Ma (23.7 %), 1551 ± 52 Ma (9.6 %), and 1467 ± 120 Ma (0.9 %) (Fig. 8H).

5 Discussion

5.1 Behavior of Rb and Sr and related Rb / Sr isotope system in muscovite from basement lithologies affected by post-crystallization hydrothermalism

The study of basement lithologies along a gradient from non-hydrothermally altered to strongly hydrothermally altered zones beneath unconformity-type uranium deposits reveals significant mineralogical, geochemical, and isotopic modifications. Across the four investigated sites, this alteration, macroscopically characterized by an apple-green color affecting the foliation planes of metapelitic gneisses, leucosomes, and granitoids, as well as filling fractures crosscutting the host lithologies (Figs. 2C, D, E, F and 4), manifests microscopically as the progressive replacement of primary and retro-metamorphic minerals (plagioclase, K-feldspars, muscovite, biotite, Fe-Mg chlorite) by an assemblage of illite and sudoite. Textural evidence suggests that these two minerals crystallized synchronously or nearly synchronously (Pacquet and Weber, 1993; Percival and Kodama, 1989). This alteration induces pronounced mineralogical transformations in both metamorphic and early hydrothermal muscovite, involving a partial to complete breakdown of their crystal structure. This process is expressed either as illitization initiated along the cleavage planes of muscovite, synchronous or quasi-synchronous with sudoite precipitation, or as massive sudoite crystallization enveloping muscovite relics (Figs. 4 and 5B). Illite-sudoite alteration constitutes the most pervasive and intense hydrothermal alteration affecting both the Athabasca Basin sandstones and the underlying basement in the vicinity of unconformity-related uranium mineralization, and has long been recognized as a robust exploration vector for U deposits (e.g., Carl et al., 1992; Derome et al., 2005; Cloutier et al., 2009; Ng et al., 2013; Martz, 2017; Kaczowka et al., 2021; Powell et al., 2022). This alteration is associated with a loss of Al, Na, K and Sr and a gain in Mg, Li and B (Martz et al., 2019a). The loss of K, Na, Al and Sr is easily explained by the K-feldspars and plagioclases replacement by illite plus sudoite. Some of these elements remain in the system and are in situ transferred to the newly-formed clays, whereas the rest leave the system. This process results from the circulation of marine-derived basinal brines, generated during early to middle diagenesis of the sedimentary basin

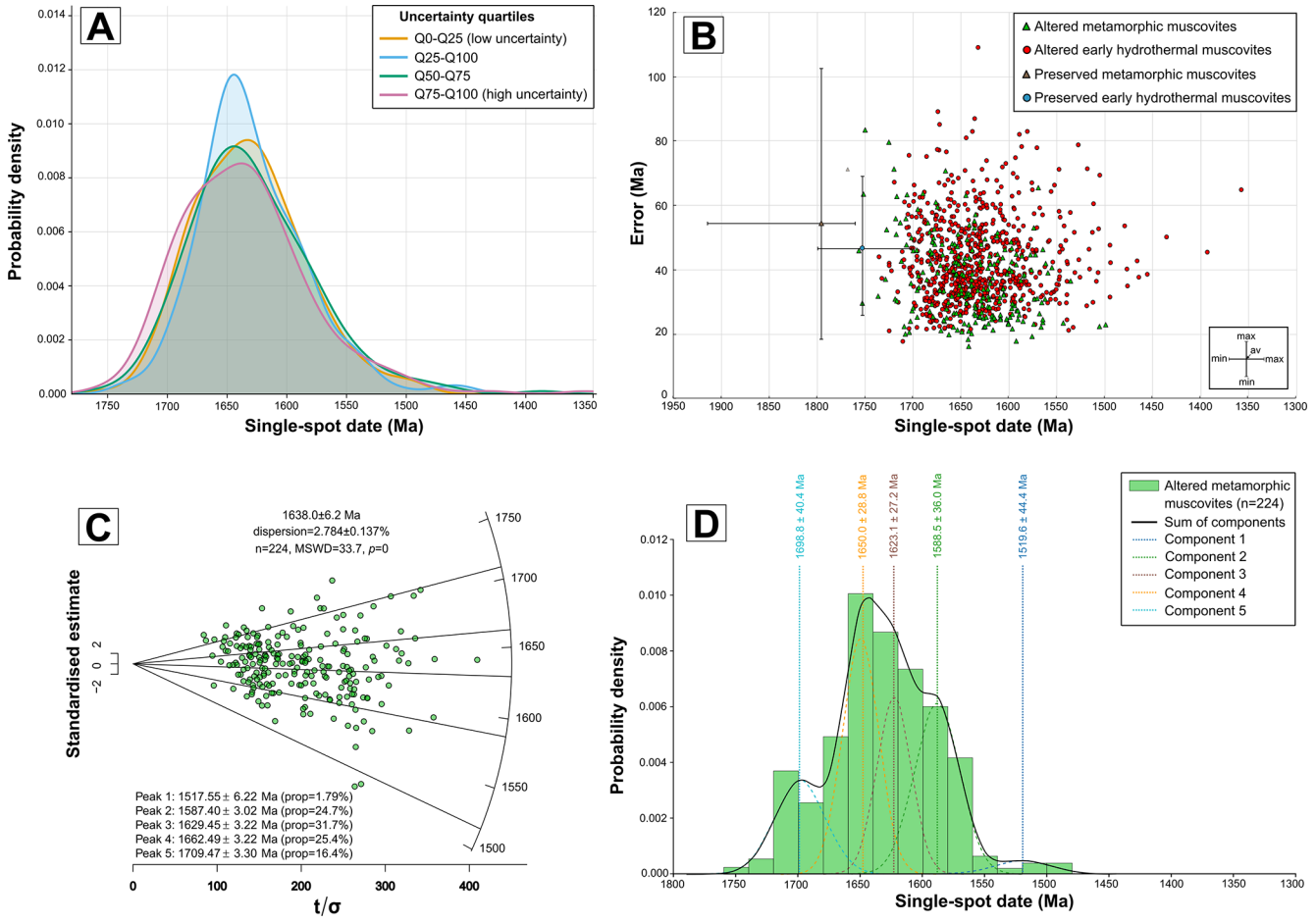

Figure 8.

(Hoeve and Sibbald, 1978; Kotzer and Kyser, 1995; Kyser et al., 2000).

This illite + sudoite assemblage formed at temperatures between 150 and 220 °C, under pressures corresponding approximately to the base of the sedimentary basin (ca. 0.1–0.3 GPa) (Halter, 1988; Kotzer and Kyser, 1995; Cloutier et al., 2009; Martz, 2017). It is associated with important chemical modifications of the host rocks, notably the loss of K, Na, Al, and Sr due to destabilization of primary feldspars and micas, and the concomitant gain in Mg, Li, B, and Ca reflecting the composition of the basinal brine and its prolonged interaction with silicates. The observed B and Mg enrichments are attributed to the intrinsic composition of the basinal fluid (Mercadier et al., 2012; Richard et al., 2011) rather than to a local metamorphic source. Variations in the illite/sudoite ratio reflect changes in thermal gradient (Beaufort et al., 2005; Kotzer and Kyser, 1995; Martz, 2017), in fluid composition (Cloutier et al., 2009), notably the K^+ / Mg^{2+} ratio, as well as in host rock lithology (Bruneton, 1993; Pacquet and Weber, 1993; Mercadier et al., 2012; Cuney and Kyser, 2015; Martz, 2017) and system pH (Kyser et al., 2000; Kister et al., 2005; Mercadier et al., 2012; Martz, 2017). The illite-sudoite alteration is not related to the recrystallization of new generations of metamorphic or early hydrothermal muscovite but instead results from fluid circulation that induces mineralogical, geochemical, and isotopic modifications. Isotopically, progressive alteration leads to systematic variations in Rb–Sr systematics, as mineralogical transformations modify both elemental concentrations and isotope ratios. The range of $^{87}Rb / ^{86}Sr$ ratios broadens from 20–670 to 5–3305, while $^{87}Sr / ^{86}Sr$ ratios shift from 1–18 to 0.8–77, with corresponding single-spot dates decreasing from 1701.9–1914.8 to 1357.0–1756.2 Ma (Fig. 9). The behaviour of the Rb–Sr geochronometer in the presence of fluid-rock interaction is best understood in terms of fluid-mediated recrystallization and open-system isotopic exchange, rather than purely thermally-activated volume diffusion (Villa, 1998; Villa, 2022).

The observed shift in Rb–Sr systematics is primarily attributed to the partial to complete loss of radiogenic ^{87}Sr from the system in response to fluid circulation associated with illite-sudoite alteration. This process results in partial to complete resetting of the Rb–Sr isotope system (Matheney et al., 1990; Kalt et al., 1994; Evans et al., 1995; Eberlei et al.,

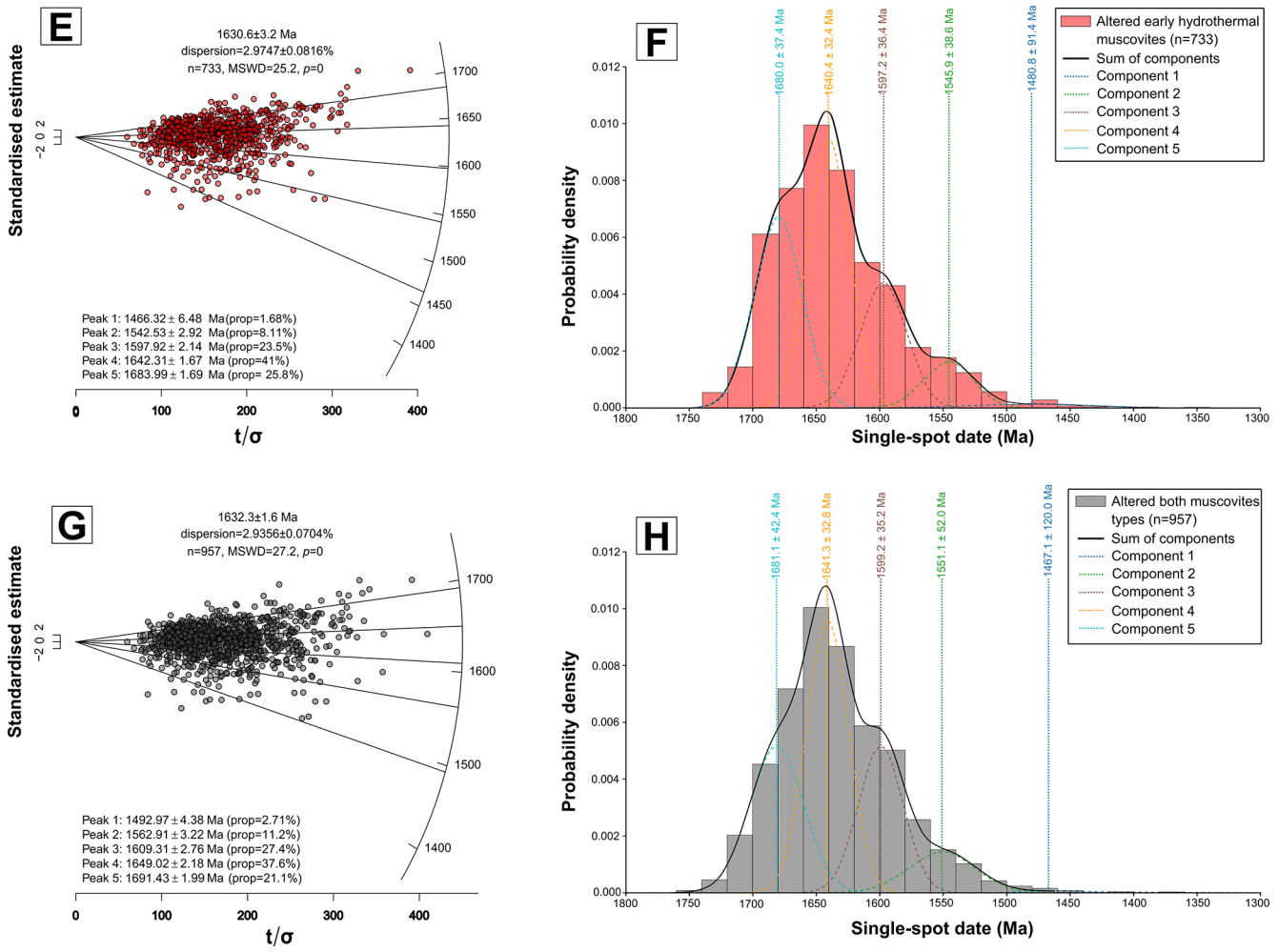

Figure 8. **(A)** Kernel density estimates (KDE) of calculated Rb–Sr single-spot dates for metamorphic and early hydrothermal muscovite affected by illite-sudoite alteration, sorted according to the quartiles of individual analytical uncertainties. The shape of the single-spot date distributions varies slightly with uncertainty level. Low uncertainties correspond to tightly clustered and homogeneous Rb–Sr single-spot dates, whereas high uncertainties are associated with greater dispersion and more pronounced asymmetry. **(B)** Scatter plot of analytical uncertainties versus Rb–Sr single-spot dates for altered metamorphic and early hydrothermal muscovite. For the preserved metamorphic and early hydrothermal muscovites, the mean values of single-spot Rb–Sr dates and their associated analytical uncertainties are reported, together with their respective maximum and minimum values. **(C)** Radial plot illustrating the dispersion of isotope ratios and calculated single-spot dates for altered metamorphic muscovite. Five statistical populations are identified in the radial plot. **(D)** Gaussian mixture model (GMM) applied to log-transformed dates, representing the distribution of Rb–Sr single-spot dates of altered metamorphic muscovite, weighted by their uncertainties, together with the five components identified by the GMM. **(E)** Radial plot showing the dispersion of isotope ratios and calculated single-spot dates for altered early hydrothermal muscovite. Five statistical populations are identified. **(F)** Gaussian mixture model applied to log-transformed dates representing the distribution of Rb–Sr single-spot dates for altered early hydrothermal muscovite, weighted by uncertainties, together with the five components identified by the GMM. **(G)** Radial plot showing the dispersion of isotope ratios and calculated single-spot dates for altered metamorphic and early hydrothermal muscovite combined. Five statistical populations are identified. **(H)** Gaussian mixture model applied to log-transformed dates representing the distribution of combined altered metamorphic and early hydrothermal muscovite Rb–Sr single-spot dates, weighted by uncertainties, as well as the five components identified by the GMM. The components identified by the GMM closely correspond to the statistical populations defined by the radial plots, taking into account the associated uncertainties. A bin width of 20 Ma was used for each GMM, consistent with the average of the individual analytical uncertainties calculated for each spot.

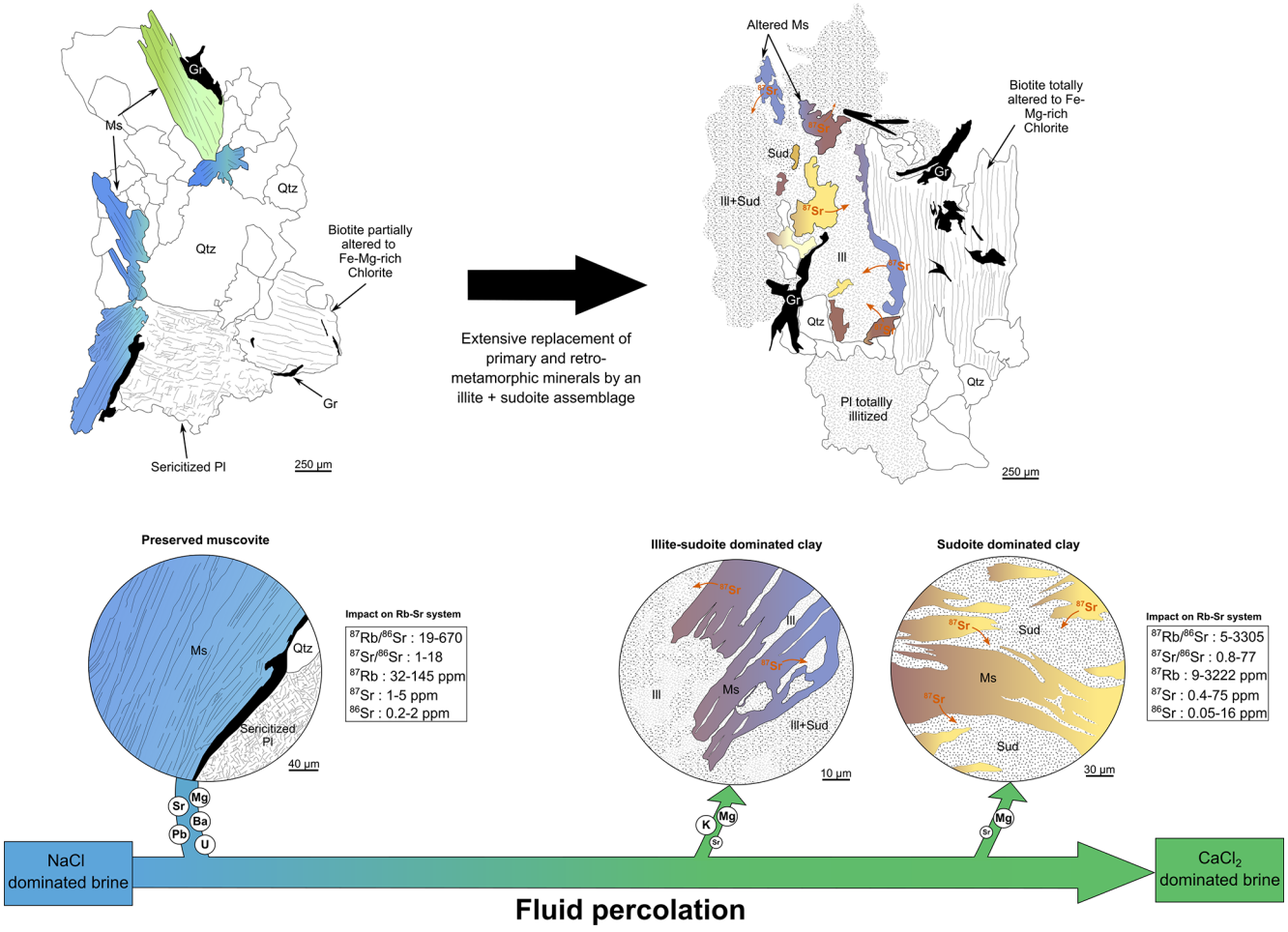

Figure 9. Schematic representation of the effect of illite-sudoite alteration on the Rb–Sr geochronometer in basement-hosted muscovite within the context of unconformity-related uranium deposits, resulting from the percolation of a Ca-Cl_2-dominated brine and fluid-rock interaction. This hydrothermal episode induces extensive replacement of primary and retro-metamorphic minerals by an illite-sudoite clay assemblage whose modal proportions vary among samples. The alteration fluid, which may circulate along pre-existing pathways generated during retro-metamorphic alteration of primary minerals, disrupts the crystal lattice of muscovite along cleavage planes. This structural breakdown leads to the loss of radiogenic ^{87}Sr from muscovite, which is redistributed into the fluid and/or the newly formed clay phases. Systematic fluid-inclusion studies (e.g., Mercadier et al., 2012; Richard et al., 2011; Martz, 2017) reveal that the regional brine, initially seawater-derived and NaCl-dominated, became progressively enriched in K, Sr, Mg, and B, and evolved toward a $CaCl_2$-dominated composition through prolonged interaction with the host rocks. This alteration episode also results in increased Rb / Sr isotope ratios in muscovite, together with elevated ^{87}Rb and ^{87}Sr contents, which may be explained by Sr loss from the muscovite molar fraction and by minor incorporation of Sr derived from either the rock matrix reservoir or the circulating fluid.

2015). Elemental maps further demonstrate that Rb is also mobile; however, the mobility of radiogenic ^{87}Sr is significantly greater than that of Rb and non-radiogenic Sr. This contrast in mobility accounts for the observed variations in both Rb / Sr ratios and Sr isotopic compositions (Fig. 5E and F) and could explain the erratic data distribution. The structural destabilization of metamorphic and early hydrothermal muscovite during hydrothermal alteration, facilitated by illitization and/or sudoitization along cleavage planes, may have enhanced diffusion and leaching of radiogenic ^{87}Sr. This process likely promoted the transfer of ^{87}Sr into clay phases and/or the fluid phase (Fig. 9). In addition, radiogenic ^{87}Sr produced in situ occupies the interlayer (I-site) in muscovite, substituting for monovalent cations such as K^+ or Rb^+ (Brigatti and Guggenheim, 2002), whereas common Sr (^{86}Sr, ^{88}Sr) is predominantly hosted in the octahedral (M-site), where divalent cations are stable. This crystallochemical distinction means that preferential removal of radiogenic ^{87}Sr from the I-site alone would be expected to drive the regression intercept toward chondritic or higher values, not toward the sub-chondritic values observed here. The anomalously low intercept values (~ 0.67) are therefore better interpreted as the result of isochron rotation under open-system conditions involving non-conservative, grain-scale redistri-

bution of both Rb and Sr (Brooks et al., 1976; Villa, 1998; Villa, 2022), rather than as a direct consequence of selective I-site ^{87}Sr loss. As demonstrated by Villa (1998, 2022), fluid-mediated recrystallization operates orders of magnitude faster than thermally-activated volume diffusion and represents the dominant mechanism of isotopic exchange in micas affected by hydrothermal fluids. In this framework, the structural destabilization of muscovite along cleavage planes during illitization and sudoitization, facilitated by the circulating Ca-Cl_2-dominated brines, promoted fluid-assisted dissolution-reprecipitation and non-conservative redistribution of Rb and Sr at the grain scale, consistent with the hygrochronological framework described by Villa (2022). The transfer of Sr into the fluid phase is independently supported by Sr enrichment documented in fluid inclusions from the Athabasca Basin brines (Mercadier et al., 2012; Richard et al., 2011; Martz, 2017).

Furthermore, the measured isotope ratios ^{87}Rb / ^{86}Sr and ^{87}Sr / ^{86}Sr, as well as ^{87}Rb and ^{87}Sr concentrations, are significantly higher in altered muscovites than in unaltered muscovites. The simultaneous increase in ^{87}Rb / ^{86}Sr and ^{87}Sr / ^{86}Sr ratios in muscovites affected by alteration or fluid circulation reflects reopening of the Rb–Sr system and selective mass redistribution of Sr during the hydrothermal event. Glodny and Grauert (2009) and Eberlei et al. (2015) demonstrate that such concurrent increases do not require mica recrystallization but rather result from a combination of dynamic fluid-rock interaction processes. These include: (i) a net loss of Sr through accelerated diffusion along defects (microfractures, cleavage planes, subgrains, dislocations), favoring the preferential loss of radiogenic Sr from transient interlayer sites or defect-related positions in muscovite; (ii) a decrease in the molar fraction of Sr, which automatically increases the ^{87}Rb / ^{86}Sr ratio since Rb is relatively immobile; and (iii) a minor incorporation of Sr, possibly more radiogenic, from the matrix reservoir or from the fluid (e.g., derived from feldspar alteration) into altered muscovite, which can slightly increase the measured ^{87}Sr / ^{86}Sr ratio.

5.2 Assessing the reliability and applicability of the Rb–Sr system in metamorphic and early hydrothermal muscovite

The characterization of well-preserved micro-domains enables the acquisition of statistically robust isotopic ages for both the metamorphic muscovite associated with the foliation of metapelitic gneisses and the early hydrothermal muscovite from anatectic granitoids or occurring in the leucosomes of metapelitic gneisses. These muscovite grains preserved from illite-sudoite alteration define well-correlated Rb–Sr regressions yielding dates of 1780.8 ± 14.6 Ma (2σ internal; ± 32 Ma including external reproducibility) and 1753.4 ± 12.4 Ma (2σ internal; ± 31 Ma including external reproducibility), respectively (Fig. 7A, B). It should be noted that in open-system Rb–Sr behaviour, fluid-rock interaction can rotate an originally valid isochron through non-conservative redistribution of Rb and Sr at the grain scale, yielding geologically meaningful slopes but mathematically anomalous intercepts that fall below physically feasible initial ^{87}Sr / ^{86}Sr values (Brooks et al., 1976; Villa, 1998; Villa, 2022). As demonstrated by Villa (1998, 2022), the isotopic perturbations formerly attributed to thermally-driven volume diffusion in micas have since been shown to reflect fluid-mediated recrystallization, which operates orders of magnitude faster than pure Fickian diffusion and represents the dominant mechanism of isotopic exchange in micas affected by hydrothermal fluids. Such rotation does not invalidate the age information recorded by the slope of the regression. However, the corresponding regression intercepts (0.6704 ± 0.0075 and 0.6989 ± 0.0168) fall below the minimum ^{87}Sr / ^{86}Sr value of the solar system (~ 0.698) and therefore cannot represent physically meaningful initial isotopic compositions. These intercepts are thus not interpreted as true initial ^{87}Sr / ^{86}Sr ratios but rather as apparent values resulting from disturbed Rb–Sr systematics. Low MSWD values (<1) and high p-values ($p \gg 0.05$) indicate strong internal coherence of the datasets, suggesting that the regressions are statistically robust despite their anomalous intercepts. Such features are characteristic of rotated or disturbed isochrons formed under open-system conditions, in which Rb and Sr are redistributed in a non-conservative manner (Brooks et al., 1976; Faure et al., 2013; Dickin, 2018). Proportional loss of Rb relative to Sr, selective Sr mobility during fluid-rock interaction, or partial isotopic resetting during metamorphism may rotate an originally valid isochron, yielding geologically reasonable slopes but non-physical intercepts (Brooks et al., 1976; DePaolo, 1981; Villa, 1998; Villa, 2022; Faure et al., 2013). The reproducibility of measured ^{87}Sr / ^{86}Sr ratios for the NIST SRM 610 reference material, together with the consistency of the regression intercept obtained for the La Posta biotite reference material, indicates that the measured ^{87}Sr / ^{86}Sr ratios and derived regression intercepts are not attributable to analytical bias or standardization issues, thereby effectively excluding an analytical or calibration-related origin. Accordingly, the anomalously low intercept values are interpreted as mathematical artefacts arising from open-system Rb–Sr behavior and isochron rotation under fluid-mediated conditions, rather than as geologically meaningful isotopic signatures or evidence of an analytical artefact. In contrast, the slopes of the regressions may still record geologically significant timing information related to muscovite crystallization or partial isotopic resetting, as has been documented in other disturbed Rb–Sr systems (Brooks et al., 1976; Villa, 1998; Villa, 2022; Zack and Hogmalm, 2016).

The single-spot ages obtained from metamorphic muscovite developed along foliation planes in Paleoproterozoic pelitic gneisses (e.g., Schneider et al., 2007; Skipton et al., 2016; Jeanneret et al., 2017; Martz, 2017) range from 1914 ± 88 to 1760 ± 30 Ma, with a modal value of

1771.2 Ma and an isochron age of 1780.8 ± 14.6 Ma (2σ internal; ±32 Ma including external reproducibility) (Fig. 10). The mean age derived from single-spot analyses, together with the isochron age, falls within the temporal window of the M2-D2 event, which generated the northeast-striking structural trend of the WMTZ and formed under a sinistral transpressional tectonic regime during the late stages of the oblique Hudsonian collision, between ca. 1813 and 1770 Ma (Fig. 10). Thermobarometric estimates indicate that rocks of the study area were re-equilibrated under conditions of ca. 0.5 GPa and 750–825 °C at this time (Annesley et al., 1992, 1997a, b, c, 1999a, b; Jeanneret et al., 2017; Toma et al., 2024). The M2–D2 temporal interval is supported by geochronological constraints derived from other mineral phases using various U–Pb chronometers, including monazite (Pb diffusion at ca. 500–800 °C; e.g., Cherniak et al., 2004; McFarlane and Harrison, 2006), zircon (>900 °C; Cherniak and Watson, 2001), and titanite (500–800 °C; Kohn, 2017). The distribution of Rb–Sr single-spot ages in metamorphic muscovite is shifted toward the lower limit of this time window (Fig. 10) and reflects the neoformation of muscovite along the retrograde $P-T$ path ($\leq\sim$ 700 °C), possibly in the presence of fluids and the cooling of muscovite below the closure temperature of the Rb–Sr system, estimated at ca. 450–600 °C (Dodson, 1973). Above this closure temperature, Sr diffusion remains sufficiently rapid to maintain an open isotope system, allowing equilibration with the surrounding matrix or between minerals.

In contrast, the single-spot ages measured in early hydrothermal muscovite crystallized within anatectic granitoids or within leucosomes of metapelitic gneisses (e.g., Schneider et al., 2007; Skipton et al., 2016; Martz, 2017) range from 1799.5 ± 42.8 to 1701.9 ± 57.6 Ma, with a mode at 1752.1 Ma and an isochron age of 1753.4 ± 12.4 Ma (2σ internal; ±31 Ma including external reproducibility) (Fig. 10). The mean age derived from single-spot analyses, together with the isochron age, falls within the temporal window of the exhumation and orogenic cooling phase of the Trans-Hudsonian orogen, a period characterized by the end of migmatization with the crystallization of leucosomes, the emplacement of leucogranitic intrusions, and the onset of hydrothermal activity associated with the cooling phase. Although its precise duration remains poorly constrained, this cooling interval is typically considered to span from ca. 1770 Ma (750 °C, 0.5 GPa) to ca. 1720 Ma (350 °C, 0.2 GPa), as documented in several studies (Annesley and Madore, 1994; Annesley et al., 1992, 1997a, b, c; Annesley et al., 2005; Jeanneret et al., 2017; Martz, 2017). The end of this period is associated with pronounced retrograde transformations, including the breakdown of cordierite to phyllosilicates, biotite chloritization, sulfide, graphite and muscovite precipitation, quartz-rich fluid circulation, and dissolution-reprecipitation of monazite and zircon (Card, 2012, 2014; Card and Noll, 2016). These processes are further constrained by cooling ages obtained from Rb–Sr biotite (Worden et al., 1985; Schneider et al., 2007), K–Ar muscovite (Philippe et al., 1993), and Ar–Ar muscovite (Alexandre et al., 2009). This timeframe has also been interpreted as reflecting a late thermal event associated with the emplacement of the Kivalliq Igneous Suite (KIS) to the northeast of the Athabasca Basin, with the Wollaston Domain being intruded by the Nueltin Granite of the same suite (ca. 1770–1730 Ma), which may have reset U–Pb metamorphic rutile ages (Adlakha and Hattori, 2021). Additionally, hydrothermal graphite, commonly spatially associated with early hydrothermal muscovite within the Wollaston-Mudjatik Transition shear zones, yields highly precise (<1 %) Re–Os isochron ages of 1731.5 ± 7.4 Ma (2σ; MSWD = 1.3). These ages are interpreted to record graphite formation during the exhumation and orogenic cooling phase of the THO (Martz, 2017) and/or a period of elevated heat flow associated with the KIS emplacement (Adlakha and Hattori, 2021), wherein aqueous fluids mobilized carbon from adjacent wall rocks into semi-brittle to brittle-ductile shear zones (Toma et al., 2022). Overall, the Rb–Sr single-spot ages of early hydrothermal muscovite are consistent with the exhumation and orogenic cooling stage of the THO, during which anatectic granitoids were emplaced and/or magmatic activity of the Kivalliq Igneous Suite occurred, and they further align with the circulation of carbon-bearing aqueous fluids responsible for the formation of hydrothermal graphite. Comparison of the Rb–Sr ages obtained from alteration-free metamorphic and early hydrothermal muscovite with existing literature datasets indicates that the Rb–Sr system constitutes a suitable geochronometer in this geological context, as evidenced by the reproducibility of comparable Rb–Sr ages across four distinct sites within the WMTZ of the THO (Fig. 10).

5.3 Assessing the reliability and applicability of the Rb–Sr system to date hydrothermal system in crystalline basement

Variably altered muscovite crystals occurring in illite-sudoite hydrothermal alteration zones in the four study sites along the WMTZ in the eastern Athabasca Basin display highly scattered Rb–Sr single-spot dates and substantial individual uncertainties, ranging from 1756.2 ± 45.8 to 1357.0 ± 64.8 Ma. Despite this variability, muscovite from both altered pelitic and granitic protoliths shows comparable Rb–Sr single spot data distributions. Gaussian Mixture Modelling (GMM) and radial plot analysis define five statistically coherent populations shared by both muscovite generations affected by illite-sudoite alteration. However, their geochronological resolution is intrinsically limited because the analytical uncertainties are large. This reflects the inherent difficulty of precisely dating Paleoproterozoic geological events, as all isotope system tend to yield significant errors at such ancient ages (e.g., Fayek and Riciputi, 2002; Alexandre et al., 2005; Rainbird et al., 2007; Schneider et al., 2007; Davis et al., 2011; Jeanneret et al., 2017; Adlakha and Hat-

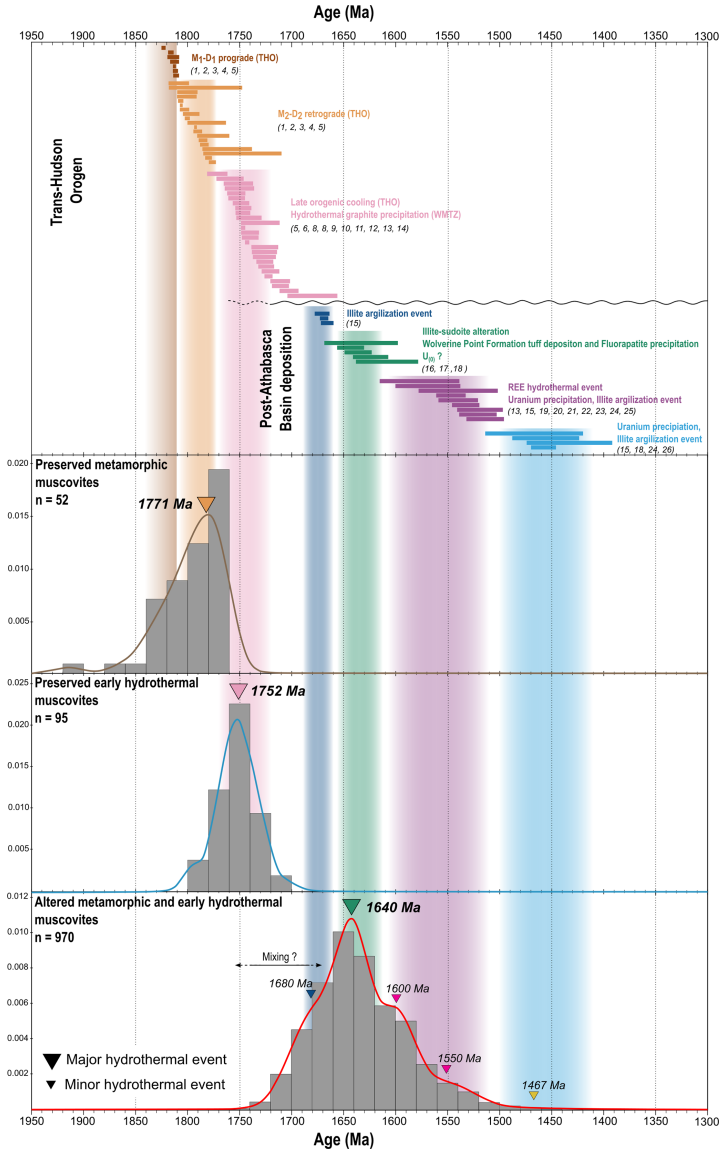

Figure 10. Compilation of published geochronological constraints for the Trans-Hudson orogen and the Athabasca Basin, integrated with the new Rb–Sr single-spot ages obtained in this study. The onset of sedimentation in the Athabasca Basin occurred at ca. 1760–1720 Ma (Ramaekers et al., 2007; Jeanneret et al., 2016). The diagram synthesizes available ages documenting the prograde metamorphic path, the retrograde evolution, and the late-orogenic cooling stages of the Trans-Hudson orogen, together with the timing of hydrothermal events recorded both in the Athabasca Basin and in its crystalline basement. Literature ages are derived from multiple minerals and chronometers. Included datasets comprise: U–Pb on zircon and monazite from (1) Annesley et al., 1992; (2) Annesley et al., 1997a, b, c; (3) Annesley et al., 1999a, b; (4) Toma et al., 2024; (5) Jeanneret et al., 2016; (6) Card, 2012; (7) Card, 2014; (8) Card and Noll, 2016); Rb–Sr on biotite from (9) Worden et al., 1985; (10) Schneider et al., 2007); U–Pb on rutile from (11) Adlakha and Hattori, 2021); Ar–Ar on muscovite from (12) Alexandre et al., 2009); K–Ar on muscovite from (13) Philippe et al., 1993); Re–Os on graphite from (14) Toma et al., 2024); Ar–Ar on illite from (15) Alexandre et al., 2009); U–Pb on zircon from (16) Rainbird et al., 2007); U–Pb on fluorapatite from (17) Davis et al., 2011); K–Ar on <2 µm fractions from gneiss from (18) Philippe et al., 1993); U–Pb on xenotime from (19) Rabiei et al., 2017); U–Pb on anatase from (20) Adlakha and Hattori, 2021); U–Pb on UO2 from (21) Alexandre et al., 2009; (22) Alexandre et al., 2005; (23) Cumming and Krstic, 1992; (24) Fayek and Riciputi, 2002; (25) McGill et al., 1993; (26) Kister, 2003). Probability density distribution and histogram plots of Rb–Sr single-spot ages obtained from preserved early hydrothermal and metamorphic muscovite unaffected by post-crystallization alteration are correlated with recognized Trans-Hudson orogenic events. Probability density distribution and histogram plots of Rb–Sr single-spot ages derived from muscovites overprinted by post-crystallization illite-sudoite alteration are presented along with the results of a Gaussian Mixture Model (GMM) used to identify distinct age components. The central age population at ca. 1640 Ma is interpreted to record the main illite-sudoite hydrothermal alteration event, whereas subordinate components may correspond to additional hydrothermal pulses documented in the literature.

tori, 2021; Toma et al., 2022). The identification of five sub-populations does not imply that this is the only possible partitioning, but rather the one favored by the model under the present configuration, given the single-spot age values and their associated uncertainties. Small sub-populations should likewise be interpreted cautiously: although they may correspond to genuine age modes, they may also reflect asymmetries, outliers, or an artificial segmentation of an otherwise continuous distribution. Several studies have demonstrated that Gaussian mixture models can generate artificial components when fitting continuous or asymmetric distributions (McLachlan and Peel, 2000; Bishop and Nasrabadi, 2006; Hastie et al., 2001). When substantial overlap exists between Gaussian components, the model often represents a single underlying population using multiple components (Fraley and Raftery, 2002). Ultimately, the components should be regarded primarily as probabilistic centers, which we attempt to compare with published datasets from the literature (Figs. 8, 10). It should be noted that BIC-based GMM algorithms tend to overestimate the number of populations with increasing sample size (Vermeesch, 2018), and that the present data are equally consistent with a smaller number of broader, partially overlapping distributions. The age components identified here are therefore not interpreted as discrete geological events but as probabilistic centers whose significance is evaluated through their correspondence with independently dated tectono-hydrothermal events documented in the regional record.

A dominant population at ca. 1640 Ma, representing the majority of the dataset and potentially overlooked without prior petrographic constraints, is consistently recorded across four independent sites within the WMTZ of the THO, supporting the regional significance and robustness of this age population. This main cluster is accompanied by subordinate age groups at ca. 1680, ca. 1600, ca. 1550 Ma, and by a minor population near ca. 1467 Ma, which display limited inter-site variability and likely reflect local heterogeneities or superimposed geological processes. These ages fall within the post-Athabasca Basin evolution, following basin deposition between ca. 1760 and 1720 Ma (Ramaekers et al., 2007; Jeanneret et al., 2016) and continuing until ca. 1541 Ma (Creaser and Stasiuk, 2007). The data obtained in strongly illite-sudoite-altered zones of the basement, spatially associated with the uranium mineralization, record extensive mineralogical transformations and major geochemical and isotopic modifications driven by the circulation of basinal brines; i.e., the same fluids responsible for the characteristic illite-sudoite alteration halos observed around all unconformity-related uranium deposits in the eastern Athabasca Basin. The spread of the Rb–Sr single-spot dates may reflect either a single, long-lived fluid-rock interaction event with a paroxysm at ca. 1640 Ma, or a sequence of pulsed hydrothermal episodes represented by the GMM and radial plot populations.

The main peak at ca. 1640 Ma is widely recognized across the basin as marking a major sedimentary reorganization event associated with a rapid westward deepening and the deposition of deeper-water successions (ca. 1664–1590 Ma; e.g., Pehrsson et al., 2023). This structural tilting correlates with the Racklan-Forward orogeny (ca. 1660–1590 Ma; e.g., Furlanetto et al., 2016; Pehrsson et al., 2023), a far-field intracontinental compressional event that reactivated deep crustal faults and deformed the northern Laurentian basement. Within the same time interval, zircon extracted from reworked tuff intraclasts of the Wolverine Point Formation (member b) yields a weighted mean $^{207}Pb/^{206}Pb$ age of 1644 ± 13 Ma (2σ), interpreted as the crystallization age of the original tuff layers (Rainbird et al., 2007; Fig. 10). These tuffs are considered to be correlative with the Yavapai and Mazatzal Paleoproterozoic orogens, particularly within the Cochise block of the Mazatzal orogen, where juvenile arc terranes and syntectonic plutons range from ca. 1660 to 1600 Ma (Sims and Peterman, 1986; Karlstrom and Bowring, 1988; Eisele and Isachsen, 2001; Rainbird et al., 2007). In a broader geodynamic framework, this event may also be linked to the Racklan Orogeny of northwestern Laurentia, interpreted as the northwestern continuation of the Mazatzal orogenic system. Together, these orogenic events define a large-scale Paleoproterozoic accretionary system that affected the margins of the Canadian Shield and promoted significant crustal reworking, consistent with the hypothesis of a circum-Laurentian orogenic belt (e.g., Furlanetto et al., 2013). U–Pb data obtained from fluorapatite in the Athabasca Basin indicate a coherent phase of phosphate cementation, constrained by weighted mean $^{207}Pb/^{206}Pb$ ages obtained on apatite with high radiogenic-to-common Pb ratios, and by Pb–Pb regression lines that are independent of common Pb (e.g., Davis et al., 2011). Fluorapatite from the Smart, Manitou Falls, and Wolverine Point formations of the Athabasca Basin yields ages of 1609 ± 30, 1638 ± 12, and 1625 ± 17 Ma, respectively, clustering around a mean age of approximately 1630 ± 9 Ma (e.g., Davis et al., 2011; Fig. 10). These ages are interpreted to record a basin-wide circulation of warm, oxidizing, P-rich brines produced by fluid-rock interactions between basinal brines and the altered crystalline basement during mesogenetic diagenesis. This large-scale fluid circulation is likely tectonically driven and related to the regional geodynamic evolution of the basin, as proposed by Pehrsson et al. (2023), and can be temporally constrained to ca. 1640 Ma based on the concordance between Rb–Sr and U–Pb apatite ages.

Taken together, these observations support the interpretation of a major basin-wide hydrothermal event at ca. 1640 Ma. Illite-sudoite alteration dated at ca. 1640 Ma can be interpreted in two alternative, but not mutually exclusive, ways. First, this alteration may predate the main stage of uranium oxide precipitation, commonly dated between ca. 1590 and 1200 Ma based on U–Pb analyses of uraninite and K–Ar/Ar–Ar geochronology of clay minerals

(Cumming and Krstic, 1992; Philippe et al., 1993; McGill et al., 1993; Fayek and Riciputi, 2002; Alexandre et al., 2009; Cloutier et al., 2011; Powell et al., 2022). In this scenario, the ca. 1640 Ma illite-sudoite alteration would represent a basin-scale hydrothermal event that prepared the basement-basin interface for subsequent uranium mineralization by enhancing permeability, redox reactivity, and uranium mobility. Alternatively, the 1640 Ma alteration may record an early phase of uranium mineralization itself, subsequently overprinted and partially reset by younger tectono-hydrothermal events. Such a model is consistent with studies demonstrating that the U–Pb systematics of uraninite and associated alteration minerals in unconformity-related uranium deposits are commonly affected by multiple fluid-flow episodes, leading to partial Pb loss and a wide dispersion of apparent ages (Kotzer and Kyser, 1990; Fayek and Kyser, 1997; Fayek et al., 2002; Fayek and Riciputi, 2002; Kyser et al., 2015). Consequently, an older hydrothermal and/or mineralizing system active during the ca. 1680–1640 Ma interval cannot be excluded, but may remain cryptic due to subsequent uranium remobilization and isotopic resetting during younger basin-wide fluid circulation events. This interpretation is further supported by analogues from northern Australia, where in situ U–Pb analyses of uraninite indicate initial mineralization or hydrothermal alteration as early as ca. 1680–1640 Ma, followed by multiple resetting episodes extending into the Mesoproterozoic and Paleozoic (Clauer et al., 2015; Skirrow et al., 2016).

In addition to the main population associated with illite-sudoite alteration at ca. 1640 Ma, several consistent statistical sub-populations are identified by the GMM. However, no chemical or mineralogical modifications are observed in the zones where these single-spot data were measured. A first sub-population calculated around ca. 1680 Ma can be interpreted in two ways. It may represent a mixed population between preserved and altered data (Fig. 6F), reflecting the onset of alteration and a partial loss of radiogenic ^{87}Sr caused by this early alteration stage at ca. 1640 Ma. Such mixing would tend to skew the single-spot Rb–Sr dates of metamorphic muscovite, which crystallized prior to early hydrothermal muscovite, toward older dates. Alternatively, this ca. 1680 Ma population could correspond to an argillization episode dated to this period by Alexandre et al. (2009) using Ar–Ar analyses on basement-hosted illite, which yields pseudo-plateau ages at McArthur River of 1669 ± 4, 1666 ± 6, and 1671 ± 7 Ma, interpreted as a pre-ore alteration event (Fig. 10). However, the actual geological significance of each published age and its attribution to a specific event are often difficult to evaluate in this context, due to successive episodes of intense fluid circulation and associated fluid-rock interaction processes that promote substantial Ar loss and consequently yield younger ages (Chi et al., 2018). Nevertheless, during this time interval, the basin is characterized by a half-graben architecture, with sediment transport predominantly directed toward the northwest and enhanced sediment accumulation along the southeastern basin margin. This configuration reflects an intracontinental extensional regime established after the THO orogeny, which may have facilitated the circulation of early fluids within the basement and may also have reset the Rb–Sr system.

The younger age populations at ca. 1600–1550 Ma are consistent with hydrothermal and mineralizing events that have been independently documented throughout the Athabasca Basin. The sub-populations at ca. 1600 Ma and ca. 1550 Ma document hydrothermal activity previously identified in the Athabasca Basin and its underlying basement, although it remains unclear whether they reflect a single event, a series of pulsatile episodes, or processes potentially related to, or distinct from, the ca. 1640 Ma event. This hydrothermal activity is highlighted in the basement by anatase precipitation, a low-pressure, low-temperature TiO2 polymorph, yielding a weighted mean $^{207}Pb/^{206}Pb$ age of 1569 ± 31 Ma (MSWD $= 0.30$, $n = 5$, 2σ; Adlakha and Hattori, 2021, Fig. 10). This age has been interpreted as reflecting the onset of oxidizing hydrothermal activity in the basement, contemporaneous with U precipitation at the world-class McArthur River deposit, which has been dated by U–Pb analyses of U oxides with two discordant ages of 1540 ± 19 Ma (Alexandre et al., 2009) and 1540 ± 38 Ma (Alexandre et al., 2005). Additional ages at ca. 1520 Ma, including 1514 ± 18 Ma (Cumming and Krstic, 1992), 1519 ± 22 Ma (Fayek and Riciputi, 2002), and 1521 ± 18 Ma (McGill et al., 1993), have been interpreted as minimum crystallization ages for primary uraninite. An episode of argillization contemporaneous with these fluid-circulation events has also been identified at 1577 ± 38 Ma (K–Ar muscovite from gneiss; Philippe et al., 1993) at Cigar Lake, and at 1533 ± 13 Ma (Ar–Ar on illite; Alexandre et al., 2009) at McArthur River. A further rare-earth-phosphate hydrothermal episode is documented in the eastern Athabasca Basin within the Maw Zone rare-earth-element deposit. U–Pb dating of xenotime yields a $^{207}Pb/^{206}Pb$ age of 1547 ± 14 Ma (Rabiei et al., 2017; Fig. 10), and both isotopic signatures and fluid-inclusion characteristics support the interpretation that the fluids responsible for xenotime precipitation were part of the same oxidizing-reducing hydrothermal system involved in the development of major uraninite mineralization across the Athabasca Basin. More broadly, these events are associated with a renewed phase of subsidence and marine flooding, attributed to intracontinental rifting or extension and linked to the emplacement of the Kuungmi Formation basalts in the adjacent Thelon Basin. This rifting episode coincides with a reorganization of the Laurentian crust following the Australia-Laurentia collision, and precedes the stabilization of Nuna, potentially promoting large-scale fluid circulation through both the basement and the basin, capable of resetting the Rb–Sr geochronometer in muscovite.

Finally, the minor age population at ca. 1467 Ma may correspond to an early mineralization event, as recorded by discordant U–Pb ages of 1467 ± 47 Ma at the Cigar Lake

deposit (Fayek and Riciputi, 2002) and by weighted mean $^{207}Pb/^{206}Pb$ ages of 1458 ± 12 Ma at the McArthur River deposit (Kister, 2003). An argillization event contemporaneous with these fluid-circulation episodes has also been identified at 1456 ± 32 Ma (K–Ar on the < 2 µm fraction from gneiss; Philippe et al., 1993) at Cigar Lake, and at 1433 ± 31 Ma (Ar–Ar on illite; Alexandre et al., 2009) at McArthur River. Overall, current data do not allow discrimination between a single protracted fluid-rock interaction episode at ca. 1640 Ma leading to the formation of an illite-sudoite alteration halo and multiple episodic fluid pulses to account for the Rb–Sr single-spot age distribution in altered metamorphic and early hydrothermal muscovite. Nevertheless, these results clearly demonstrate the applicability of the Rb–Sr chronometer for constraining hydrothermal fluid circulation at basin-basement interfaces. The distinct age populations identified in muscovite and alteration products correspond to tectono-hydrothermal events that are independently recognized in the regional geological record and have been previously dated using other geochronological methods. Comparable multi-stage fluid-thermal histories have been documented in other hydrothermal systems, such as gold deposit systems, where primary mineral phases commonly preserve evidence for repeated isotopic resetting, trace-element redistribution, and microstructural overprinting associated with episodic fluid and heat input (e.g., Bevan et al., 2021; Chen et al., 2024; Drake et al., 2023; Huang et al., 2023; Liu et al., 2018; Mao et al., 2013; Olierook et al., 2020; Redaa et al., 2021, 2022; Şengün et al., 2019; Wang et al., 2022; Zametzer et al., 2022; Tian et al., 2024; Boschetti et al., 2025; Huang et al., 2025). Such behaviour underscores the capacity of mineral-scale chronometers to resolve protracted hydrothermal evolution. In this context, the present data suggest that the Rb–Sr system in muscovite and alteration minerals is sensitive to successive hydrothermal events at basin-basement interfaces, highlighting its potential as a robust tool for reconstructing the timing and duration of fluid circulation processes, while emphasizing the need for further work to evaluate mineralogical and geochemical controls on system behaviour. Although these initial results are promising, further work is required to assess potential mineralogical or geochemical specificities that may influence the Rb–Sr system under such conditions.

6 Conclusions

This study tests the relevance and limitations of the Rb–Sr chronometer applied to muscovite from pelitic gneisses, including migmatites, and granitoids from the Paleoproterozoic basement of the Wollaston-Mudjatik Transition Zone, within the context of hydrothermal alteration (formed by an association of illite and sudoite) associated with the formation of Athabasca Basin unconformity-related uranium deposits. The primary objective was to determine to what extent this isotope system, conventionally used to date the crystallization or cooling of crustal rocks, can also record and quantify late-stage fluid circulation events, despite the complexity induced by partial system reopening through fluid-rock interaction.

Petrographic and isotopic analyses of preserved domains demonstrate that, in areas lacking illite-sudoite alteration, metamorphic and early hydrothermal muscovite yield ages of ca. 1780 and ca. 1750 Ma, respectively. Retro-metamorphic muscovite specifically records the transition to temperatures below its closure temperature (450–600 °C), marking cooling, possibly in the presence of fluids, following the peak metamorphism and isothermal decompression of the THO basement. Early hydrothermal muscovite, in turn, records the exhumation and orogenic cooling phase of the THO, during which anatectic granitoids were emplaced and/or magmatic activity of the Kivalliq Igneous Suite occurred. Its formation is also consistent with the circulation of carbon-bearing aqueous fluids that facilitated the development of hydrothermal graphite. These results demonstrate that, in minimally altered domains, the Rb–Sr system yields ages consistent with established geochronological constraints obtained from independent isotope system and mineral phases for both episodes, thereby confirming that the Rb–Sr chronometer remains fully reliable for dating the terminal Paleoproterozoic thermo-metamorphic events.

In contrast, muscovite from pelitic gneiss or granitic protoliths affected by illite-sudoite alteration developed after the deposition of the Athabasca Basin displays deeply modified mineralogical, geochemical, and isotopic signatures. These signatures reflect the micrometre-scale reopening of the Rb–Sr isotope system through fluid-rock interaction during brine circulation, in response to the structural destabilization of muscovite during illitization and/or sudoitization. The preferential transfer of radiogenic ^{87}Sr into clay phases and/or the fluid phase constitutes the major mechanism driving isotopic resetting.

The dominant population of Rb–Sr single spot data at ca. 1640 Ma reflects a major hydrothermal event. This age interval coincides with a first-order sedimentary reorganization of the basin and with crustal-scale reactivation related to the late Paleoproterozoic Racklan-Mazatzal orogenic system (ca. 1660–1590 Ma), which affected the northwestern to southern margins of Laurentia and the adjacent edge of the Canadian Shield. These tectonic processes are accompanied by widespread fluid circulation and diagenetic to hydrothermal events in the Athabasca Basin, as independently documented by U–Pb ages obtained on fluorapatite. Comparison with other geochronological constraints and regional geodynamic reconstructions supports the interpretation that the ages measured on altered muscovite and associated alteration products are geologically meaningful and temporally consistent. Rather than reflecting localized or spurious resetting, these ages are best interpreted as recording a geologically realistic and regionally significant hydrothermal event,

broadly coeval with the Racklan-Mazatzal orogenic continuum, which represents the northwestern expression of a circum-Laurentian orogenic belt affecting the margins of the Canadian Shield. It corresponds to the principal illite-sudoite alteration event responsible for the mineralized halos around uranium deposits and represents the key event recorded by altered muscovites. Additional age populations reflect further hydrothermal episodes or fluid-reactivation phases: (i) ca. 1680 Ma, possibly linked to a pre-ore argillization event documented by Ar–Ar ages on illite, or to an initial stage of partial disturbance of the Rb–Sr system; (ii) ca. 1600 and ca. 1550 Ma, corresponding to a major oxidizing hydrothermal phase concomitant with a mineralizing event, recognized from U–Pb ages on anatase, xenotime, and uraninite, notably at McArthur River; (iii) ca. 1467 Ma, associated with a major mineralizing episode recorded in the district (Cigar Lake).

This study demonstrates that the in situ Rb–Sr geochronometer applied to muscovite and related alteration products constitutes a relevant tool not only for constraining late-metamorphic and late-magmatic and/or early hydrothermal histories in unaltered domains, but also for identifying and dating post-crystallization hydrothermal circulation events after basin sedimentation, associated with unconformity-related metal deposits. By coupling detailed petrographic analysis with in situ geochemical characterization, it becomes possible to distinguish preserved ages reflecting Paleoproterozoic crystallization or cooling from reset ages marking Mesoproterozoic hydrothermal episodes. The Rb–Sr chronometer thus emerges as a powerful and complementary tool within the existing suite of fluid tracers, opening new perspectives for the temporal and spatial reconstruction of paleo-hydrothermal systems across basin-basement interfaces.

Data availability. All data supporting the findings of this study are provided in the Appendix.

Supplement. The supplement related to this article is available online at https://doi.org/10.5194/gchron-8-387-2026-supplement.

Author contributions. Conceptualization: QB, JM; Fieldwork: QB, GM, EF, TO, AK, JM; Methodology and data acquisition: QB, CP, AL, JM; Data curation: QB, MS, TO, CP, AL, JM; Writing (original draft preparation): QB, GM, EF, CB, AL, PM, JM; Funding acquisition: JM.

Competing interests. The contact author has declared that none of the authors has any competing interests.

Disclaimer. Publisher's note: Copernicus Publications remains neutral with regard to jurisdictional claims made in the text, published maps, institutional affiliations, or any other geographical representation in this paper. The authors bear the ultimate responsibility for providing appropriate place names. Views expressed in the text are those of the authors and do not necessarily reflect the views of the publisher.

Acknowledgements. The French Agence Nationale de la Recherche (ANR) and Orano are thanked for funding this project. The authors gratefully acknowledge Orano Canada and Cameco for providing access to the field sites, samples, and data transfer. Special thanks are extended to Charles Khairallah, Magdalena Anderson, Andrew Kaczowka, and Gerard Zaluski for their valuable assistance during the field missions and data sharing. The authors would like to thank the editor Klaus Mezger, the associate editor Noah M. McLean, and two reviewers (Jarred Lloyd and one anonymous reviewer) for their constructive comments and suggestions, which greatly improved the quality of this manuscript.

Financial support. This research has been supported by the French Agence Nationale de la Recherche (ANR) and Orano, under grant no. ANR-21-CHIN-0006 (project GeomIn3D).

Review statement. This paper was edited by Noah M McLean and reviewed by Jarred Lloyd and one anonymous referee.

References

Adlakha, E. E. and Hattori, K.: Compositional variation and timing of aluminum phosphate-sulfate minerals in the basement rocks along the P2 fault and in association with the McArthur River uranium deposit, Athabasca Basin, Saskatchewan, Canada, Am. Mineral., 100, 1386–1399, https://doi.org/10.2138/am-2015-5069, 2015.

Adlakha, E. and Hattori, K.: Thermotectonic events recorded by U–Pb geochronology and Zr-in-rutile thermometry of Ti oxides in basement rocks along the P2 fault, eastern Athabasca Basin, Saskatchewan, Canada, Geol. Soc. Am. Bull., 134, 567–576, https://doi.org/10.1130/B35820.1, 2021.

Aldega, L., Viola, G., Casas-Sainz, A., Marcén, M., Román-Berdiel, T., and van der Lelij, R.: Unraveling Multiple Thermotectonic Events Accommodated by Crustal-Scale Faults in Northern Iberia, Spain: Insights From K–Ar Dating of Clay Gouges, Tectonics, 38, 3629–3651, https://doi.org/10.1029/2019TC005585, 2019.

Alexandre, P., Kyser, K., Polito, P., and Thomas, D.: Alteration mineralogy and stable isotope geochemistry of Paleoproterozoic basement-hosted unconformity-type uranium deposits in the Athabasca Basin, Canada, Econ. Geol., 100, 1547–1563, https://doi.org/10.2113/gsecongeo.100.8.1547, 2005.

Alexandre, P., Kyser, K., Thomas, D., Polito, P., and Marlat, J.: Geochronology of unconformity-related uranium deposits in the Athabasca Basin, Saskatchewan, Canada and their integration in the evolution of the basin, Miner. Deposita, 44, 41-59, https://doi.org/10.1007/s00126-007-0153-3, 2009.

Alexandre, P., Jiricka, D., and Witt, G.: Formation and evolution of the Centennial unconformity-related uranium deposit in the south-central Athabasca Basin, Canada, Econ. Geol., 107, 385–400, https://doi.org/10.2113/econgeo.107.3.385, 2012.

Anders, M. H., Laubach, S. E., and Scholz, C. H.: Microfractures: A review, J. Struct. Geol., 69, 377–394, https://doi.org/10.1016/j.jsg.2014.05.011, 2014.

Ansdell, K. M.: Tectonic evolution of the Manitoba-Saskatchewan segment of the Paleoproterozoic Trans-Hudson Orogen, Canada, Can. J. Earth Sci., 42, 741–759, https://doi.org/10.1139/e05-035, 2005.

Annesley, I., Madore, C., and Krogh, T. E.: U–Pb zircon, titanite, and monazite ages from the Wollaston Domain: A summary, Summary of Investigations, Saskatchewan Geological Survey, Saskatchewan Energy and mines, Miscellaneous Report 92-4, 61–65, https://pubsaskdev.blob.core.windows.net/pubsask-prod/88117/88117-Annesley-Madore-Krogh_1992_MiscRep92-4.pdf (last access: 3 July 2026), 1992.

Annesley, I. R. and Madore, C.: A geological study of the Wollaston-Mudjatik domain boundary in the Wollaston Lake area, Hearne Province, Saskatchewan, Saskatchewan Research Council, Publ. R-1230-6-C-94, 162 pp., https://scholar-google-com.bases-doc.univ-lorraine.fr/citations?view_op=view_citation&hl=fr&user=b-WIUOcAAAAJ&cstart=100&pagesize=100&sortby=pubdate&citation_for_view=b-WIUOcAAAAJ:k_IJM867U9cC (last access: 3 July 2026), 1994.

Annesley, I. R., Madore, C., and Shi, R.: Thermotectonic evolution of the Wollaston EAGLE Project Area, Saskatchewan Research Council, Publ. R-1420-2-C-97, Part 1, 1–62, https://scholar-google-com.bases-doc.univ-lorraine.fr/citations?view_op=view_citation&hl=fr&user=b-WIUOcAAAAJ&cstart=100&pagesize=100&sortby=pubdate&citation_for_view=b-WIUOcAAAAJ:CHSYGLWDkRkC (last access: 3 July 2026), 1997a.

Annesley, I., Madore, C., Shi, R., and Krogh, T.: U–Pb geochronology of thermotectonic events in the Wollaston Lake area, Wollaston Domain: A summary of 1994–1996 results, Summary of Investigations 1997, Saskatchewan Geological Survey, Saskatchewan Energy and Mines, 1, 162–173, https://www.researchgate.net/publication/273767482_U-Pb_geochronology_of_thermotectonic_events_in_the_Wollaston_Lake_area_Wollaston_Domain_A_summary_of_1994-1996_results (last access: 3 July 2026), 1997b.

Annesley, I. R., Madore, C., and Krogh, T. E.: U–Pb geochronology of peraluminous pegmatites from theWollaston Lake area, northern Saskatchewan, Geol. Assoc. Can.-Mineral. Assoc. Can. Annual Meeting, Program with Abstracts, 22, A-4, 1997c.

Annesley, I. R., Madore, C., Shi, R., and Krogh, T. E: U–Pb geochronology and thermotectonic history ofthe Wollaston Domain in the Wollaston Lake area, Hearne Province, Saskatchewan, Geol. Assoc. Can.-Mineral. Assoc. Can. Annual Meeting, Program with Abstracts, 21, A-4, 1999a.

Annesley, I. R., Madore, C., Krogh, T. E., Kwok, Y. Y., and Kamo, S. L.: New U–Pb zircon and monazitegeochronological results for Archean and Paleoproterozoic basement to the southeastern part of the AthabascaBasin, Saskatchewan, Saskatchewan Geological Survey, Misc. Rep. 99-4.2, 90–99, https://www.researchgate.net/publication/273695990_New_U-Pb_zircon_and_monazite_geochronological_results_for_Archean_and_Paleoproterozoic_basement_to_the_southeastern_part_of_the_Athabasca_Basin (last access: 3 July 2026), 1999b.

Annesley, I. R., Madore, C., and Portella, P.: Geology and thermotectonic evolution of the western margin of the Trans-Hudson Orogen: evidence from the eastern sub-Athabasca basement, Saskatchewan, Can. J. Earth Sci., 42, 573–597, https://doi.org/10.1139/e05-034, 2005.

Beaufort, D., Patrier, P., Laverret, E., Bruneton, P., and Mondy, J.: Clay Alteration Associated with Proterozoic Unconformity-Type Uranium Deposits in the East Alligator Rivers Uranium Field, Northern Territory, Australia, Econ. Geol., 100, 515–536, https://doi.org/10.2113/gsecongeo.100.3.515, 2005.

Bevan, D., Coath, C. D., Lewis, J., Schwieters, J., Lloyd, N., Craig, G., Wehrs, H., and Elliott, T.: In situ Rb–Sr dating by collision cell, multicollection inductively-coupled plasma mass-spectrometry with pre-cell mass-filter, (CC-MC-ICPMS/MS), J. Anal. Atom. Spectrom., 36, 917–931, https://doi.org/10.1039/D1JA00006C, 2021.

Boiron, M.-C., Cathelineau, M., and Richard, A.: Fluid flows and metal deposition near basement /cover unconformity: lessons and analogies from Pb-Zn-F-Ba systems for the understanding of Proterozoic U deposits, Geofluids, 10, 270–292, https://doi.org/10.1111/j.1468-8123.2010.00289.x, 2010.

Boschetti, L., Boullerne, C., Rolland, Y., Schwartz, S., Milesi, G., Bienveignant, D., Macret, E., Charpentier, D., Münch, P., Mercadier, J., Iemmolo, A., Lanari, P., Rossi, M., and Mouthereau, F.: Shear zone memory revealed by in-situ Rb–Sr and $^{40}Ar/^{39}Ar$ dating of Pyrenean and Alpine tectonic phases in the external Alps, Lithos, 514–515, 108168, https://doi.org/10.1016/j.lithos.2025.108168, 2025.

Bickford, M., Chiarenzelli, J., Van Schmus, W., Collerson, K. D., and Lewry, J.: Proterozoic collisional tectonism in the Trans-Hudson orogen, Saskatchewan, Geology, 18, 14–18, 1990.

Bickford, M. E., Mock, T. D., Steinhart Iii, W. E., Collerson, K. D., and Lewry, J. F.: Origin of the Archean Sask craton and its extent within the Trans-Hudson orogen: evidence from Pb and Nd isotopic compositions of basement rocks and post-orogenic intrusions, Can. J. Earth Sci., 42, 659–684, https://doi.org/10.1139/e04-064, 2005.

Bishop, C. M. and Nasrabadi, N. M.: Pattern recognition and machine learning, Springer, ISBN 978-0-387-31073-2, 2006.

Brigatti, M. F. and Guggenheim, S.: Mica Crystal Chemistry and the Influence of Pressure, Temperature, and Solid Solution on Atomistic Models, Rev. Mineral. Geochem., 46, 1–97, https://doi.org/10.2138/rmg.2002.46.01, 2002.

Brooks, C., Hart, S. R., Hofmann, A., and James, D. E.: Rb–Sr mantle isochrons from oceanic regions, Earth Planet. Sc. Lett., 32, 51–61, https://doi.org/10.1016/0012-821X(76)90184-9, 1976.

Bruneton, P.: Geological environment of the Cigar Lake uranium deposit, Can. J. Earth Sci., 30, 653–673, https://doi.org/10.1139/e93-054, 1993.

Campanha, G. A. C., Hueck, M., Wemmer, K., Esteves, M. C. B., Joncew, H. C., Faleiros, F. M., and Veloso, R. S. S.: Foreland deformation of Brasiliano orogens at the eastern and western margins of the São Francisco Craton: K–Ar illite dating of the

Araçuaí and Brasília fold-and-thrust belts, J. Geol. Soc., 183, jgs2025-138, https://doi.org/10.1144/jgs2025-138, 2025.

Card, C.: The Origins of Anomalously Graphitic Rocks and Quartzite Ridges in the Basement to the Southeastern Athabasca Basin, https://www.researchgate.net/publication/272175876_The_Origins_of_Anomalously_Graphitic_Rocks_and_Quartzite_Ridges_in_the_Basement_to_the_Southeastern_Athabasca_Basin (last access: 3 July 2026), 2012.

Card, C.: Altered Pelitic Gneisses and Associated "Quartzite Ridges" Beneath the Southeastern Athabasca Basin: Alteration Facies and their Relationship to Uranium Deposits along the Wollaston-Mudjatik Transition, https://www.researchgate.net/publication/272175864_Altered_Pelitic_Gneisses_and_Associated_Quartzite_Ridges_Beneath_the_Southeastern_Athabasca_Basin_Alteration_Facies_and_their_Relationship_to_Uranium_Deposits_along_the_Wollaston-Mudjatik_Transition (last access: 3 July 2026), 2014.

Card, C. and Noll, J.: Host-Rock Protoliths, Pre-Ore Metasomatic Mineral Assemblages and Textures, and Exotic Rocks in the Western Athabasca Basin: Ore-System Controls and Implications for the Unconformity-Related Uranium Model, in: Summary of Investigations 2016, 2, Saskatchewan Geological Survey, Sask. Ministry of the Economy, Misc. Rep. 2016-4.2, https://doi.org/10.13140/RG.2.2.26473.70241, 2016.

Carl, C., Pechmann, E. V., Höhndorf, A., and Ruhrmann, G.: Mineralogy and U/Pb, Pb/Pb, and Sm/Nd geochronology of the Key Lake uranium deposit, Athabasca Basin, Saskatchewan, Canada, Can. J. Earth Sci., 29, 879–895, https://doi.org/10.1139/e92-075, 1992.

Cathelineau, M., Boiron, M.-C., Fourcade, S., Ruffet, G., Clauer, N., Belcourt, O., Coulibaly, Y., Banks, D. A., and Guillocheau, F.: A major Late Jurassic fluid event at the basin/basement unconformity in western France: $^{40}Ar/^{39}Ar$ and K–Ar dating, fluid chemistry, and related geodynamic context, Chem. Geol., 322–323, 99–120, https://doi.org/10.1016/j.chemgeo.2012.06.008, 2012.

Chen, M., Chen, G., An, P., Zhang, L., and Wang, Y.: In situ illite Rb–Sr dating indicates the coevality of Carlin-type gold deposits inside and around the isolated carbonate platform in western Guangxi, China, Ore Geol. Rev., 165, 105905, https://doi.org/10.1016/j.oregeorev.2024.105905, 2024.

Cherniak, D. J. and Watson, E. B.: Pb diffusion in zircon, Chem. Geol., 172, 5–24, https://doi.org/10.1016/S0009-2541(00)00233-3, 2001.

Cherniak, D. J., Watson, E. B., Grove, M., and Harrison, T. M.: Pb diffusion in monazite: a combined RBS/SIMS study, Geochim. Cosmochim. Ac., 68, 829-840, https://doi.org/10.1016/j.gca.2003.07.012, 2004.

Chi, G., Li, Z., Chu, H., Bethune, K. M., Quirt, D. H., Ledru, P., Normand, C., Card, C., Bosman, S., Davis, W. J., and Potter, E. G.: A SHALLOW-BURIAL MINERALIZATION MODEL FOR THE UNCONFORMITY-RELATED URANIUM DEPOSITS IN THE ATHABASCA BASIN, Econ. Geol., 113, 1209–1217, https://doi.org/10.5382/econgeo.2018.4588, 2018.

Chiarenzelli, J.: Petrogenesis and tectonic significance of the Guncoat and Nistowiak gneisses, Glennie Lake Domain, northern Saskatchewan, unpublished PhD thesis, University of Kansas, 229, 1989.

Chiarenzelli, J., Aspler, L., Villeneuve, M., and Lewry, J.: Early Proterozoic Evolution of the Saskatchewan Craton and Its Allochthonous Cover, Trans-Hudson Orogen, J. Geol., 106, 247–268, https://doi.org/10.1086/516020, 1998.

Clauer, N., Środoń, J., Francu, J., and Šucha, V.: K–Ar dating of illite fundamental particles separated from illite-smectite, Clay Miner., 32, 181–196, https://doi.org/10.1180/claymin.1997.032.2.02, 1997.

Clauer, N., Mercadier, J., Patrier, P., Laverret, E., and Bruneton, P.: Relating unconformity-type uranium mineralization of the Alligator Rivers Uranium Field (Northern Territory, Australia) to the regional Proterozoic tectono-thermal activity: An illite K–Ar dating approach, Precambrian Res., 269, 107–121, https://doi.org/10.1016/j.precamres.2015.08.007, 2015.

Cloutier, J., Kyser, K., Olivo, G. R., Alexandre, P., and Halaburda, J.: The Millennium Uranium Deposit, Athabasca Basin, Saskatchewan, Canada: An Atypical Basement-Hosted Unconformity-Related Uranium Deposit, Econ. Geol., 104, 815–840, https://doi.org/10.2113/gsecongeo.104.6.815, 2009.

Cloutier, J., Kyser, K., Olivo, G. R., and Brisbin, D.: Geochemical, isotopic, and geochronlologic constraints on the formation of the Eagle Point basement-hosted uranium deposit, Athabasca Basin, Saskatchewan, Canada and recent remobilization of primary uraninite in secondary structures, Miner Deposita, 46, 35–56, https://doi.org/10.1007/s00126-010-0308-5, 2011.

Corrigan, D.: Paleoproterozoic crustal evolution and tectonics processes: Insights from the LITHOPROBE program in the Trans-Hudson orogen, Canada, Tectonic Styles in Canada: The LITHOPROBE Perspective, 49, 237–284, 2012.

Corrigan, D., Hajnal, Z., Németh, B., and Lucas, S. B.: Tectonic framework of a Paleoproterozoic arc-continent to continent-continent collisional zone, Trans-Hudson Orogen, from geological and seismic reflection studies, Can. J. Earth Sci., 42, 421–434, https://doi.org/10.1139/e05-025, 2005.

Corrigan, D., Pehrsson, S., Wodicka, N., and De Kemp, E.: The Palaeoproterozoic Trans-Hudson Orogen: a prototype of modern accretionary processes, in: Ancient Orogens and Modern Analogues, edited by: Murphy, J. B., Keppie, J. D., and Hynes, A. J., Geological Society of London, Special Publication 327, 457–479, https://doi.org/10.1144/SP327.19, 2009

Creaser, R. and Stasiuk, L. D.: Depositional age of the Douglas Formation, Northern Saskatchewan, determined by Re-Os geochronology, Bulletin of the Geological Survey of Canada, 588, 341–346, https://doi.org/10.4095/223779, 2007.

Cumming, G. L. and Krstic, D.: The age of unconformity-related uranium mineralization in the Athabasca Basin, northern Saskatchewan, Can. J. Earth Sci., 29, 1623–1639, https://doi.org/10.1139/e92-128, 1992.

Cuney, M. and Kyser, K.: Geology and geochemistry of uranium and thorium deposits, Mineralogical Association of Canada, https://doi.org/10.3749/9780921294726, 2015.

DePaolo, D. J.: Trace element and isotopic effects of combined wallrock assimilation and fractional crystallization, Earth Planet. Sc. Lett., 53, 189–202, https://doi.org/10.1016/0012-821X(81)90153-9, 1981.

Derome, D., Cathelineau, M., Cuney, M., Fabre, C., Lhomme, T., and Banks, D. A.: Mixing of Sodic and Calcic Brines and Uranium Deposition at McArthur River, Saskatchewan, Canada: A Raman and Laser-Induced Breakdown Spectro-

scopic Study of Fluid Inclusions, Econ. Geol., 100, 1529–1545, https://doi.org/10.2113/gsecongeo.100.8.1529, 2005.

Davis, W., Gall, Q., Jefferson, C. W., and Rainbird, R.: Fluorapatite in the Paleoproterozoic Thelon Basin: Structural-stratigraphic context, in situ ion microprobe U–Pb ages, and fluid-flow history, Geol. Soc. Am. Bull., 123, 1056–1073, https://doi.org/10.1130/B30163.1, 2011.

Dickin, A. P.: Radiogenic Isotope Geology, 3rd ed., Cambridge University Press, https://doi.org/10.1017/9781316163009, 2018.

Dodson, M. H.: Closure temperature in cooling geochronological and petrological systems, Contr. Mineral. Petrol., 40, 259–274, https://doi.org/10.1007/BF00373790, 1973.

Drake, H., Tillberg, M., Reinhardt, M., Whitehouse, M. J., and Kooijman, E.: In Situ Rb / Sr Geochronology and Stable Isotope Geochemistry Evidence for Neoproterozoic and Paleozoic Fracture-Hosted Fluid Flow and Microbial Activity in Paleoproterozoic Basement, SW Sweden, Geochem. Geophy. Geosy., 24, e2023GC010892, https://doi.org/10.1029/2023GC010892, 2023.

Eberlei, T., Habler, G., Wegner, W., Schuster, R., Körner, W., Thöni, M., and Abart, R.: Rb / Sr isotopic and compositional retentivity of muscovite during deformation, Lithos, 227, 161–178, https://doi.org/10.1016/j.lithos.2015.04.007, 2015.

Eisele, J. and Isachsen, C. E.: Crustal Growth in Southern Arizona: U–Pb Geochronologic and Sm-Nd Isotopic Evidence for Addition of the Paleoproterozoic Cochise Block to the Mazatzal Province, Am. J. Sci., 301, 773–797, https://doi.org/10.2475/ajs.301.9.773, 2001.

Etheridge, M. A., Wall, V. J., and Vernon, R. H.: The role of the fluid phase during regional metamorphism and deformation, J. Metamorph. Geol., 1, 205–226, https://doi.org/10.1111/j.1525-1314.1983.tb00272.x, 1983.

Evans, J., MILLAR, I., and NOBLE, S.: Hydration during uplift is recorded by reset Rb–Sr whole-rock ages, J. Geol. Soc., 152, 209–212, https://doi.org/10.1144/gsjgs.152.2.0209, 1995.

Faulkner, D. R., Jackson, C. A. L., Lunn, R. J., Schlische, R. W., Shipton, Z. K., Wibberley, C. A. J., and Withjack, M. O.: A review of recent developments concerning the structure, mechanics and fluid flow properties of fault zones, J. Struct. Geol., 32, 1557–1575, https://doi.org/10.1016/j.jsg.2010.06.009, 2010.

Faure, G. and Mensing, T. M.: Isotopes: Principles and Applications, Third edition, John Wiley & Sons, Inc, Hoboken, New Jersey, ISBN 978-0-471-38437-3, 897 pp., 2013.

Fayek, M. and Kyser, T. K.: Characterization of multiple fluid-flow events and rare-earth-element mobility associated with formation of unconformity-type uranium deposits in the Athabasca Basin, Saskatchewan, Can. Mineral., 35, 627–658, 1997.

Fayek, M. and Riciputi, L.: U and Pb isotope analysis of uranium minerals by ion microprobe and the geochronology of McArthur River and Sue Zone uranium deposits, Saskatchewan, Canada, Can. Mineral., 40, 1553–1569, https://doi.org/10.2113/gscanmin.40.6.1553, 2002.

Fayek, M., Harrison, T. M., Ewing, R. C., Grove, M., and Coath, C. D.: O and Pb isotopic analyses of uranium minerals by ion microprobe and U–Pb ages from the Cigar Lake deposit, Chem. Geol., 185, 205–225, https://doi.org/10.1016/S0009-2541(01)00401-6, 2002.

Fraley, C. and Raftery, A. E.: Model-Based Clustering, Discriminant Analysis, and Density Estimation, J. Am. Stat. Assoc., 97, 611–631, https://doi.org/10.1198/016214502760047131, 2002.

Frey, M., Bossennec, C., Seib, L., Bär, K., Schill, E., and Sass, I.: Interdisciplinary fracture network characterization in the crystalline basement: a case study from the Southern Odenwald, SW Germany, Solid Earth, 13, 935–955, https://doi.org/10.5194/se-13-935-2022, 2022.

Furlanetto, F., Thorkelson, D. J., Daniel Gibson, H., Marshall, D. D., Rainbird, R. H., Davis, W. J., Crowley, J. L., and Vervoort, J. D.: Late Paleoproterozoic terrane accretion in northwestern Canada and the case for circum-Columbian orogenesis, Precambrian Res., 224, 512–528, https://doi.org/10.1016/j.precamres.2012.10.010, 2013.

Furlanetto, F., Thorkelson, D. J., Rainbird, R. H., Davis, W. J., Gibson, H. D., and Marshall, D. D.: The Paleoproterozoic Wernecke Supergroup of Yukon, Canada: Relationships to orogeny in northwestern Laurentia and basins in North America, East Australia, and China, Gondwana Res., 39, 14–40, https://doi.org/10.1016/j.gr.2016.06.007, 2016.

Galbraith, R. F.: Graphical Display of Estimates Having Differing Standard Errors, Technometrics, 30, 271–281, https://doi.org/10.2307/1270081, 1988.

Galbraith, R. F.: The radial plot: Graphical assessment of spread in ages, International Journal of Radiation Applications and Instrumentation. Part D. Nuclear Tracks and Radiation Measurements, 17, 207–214, https://doi.org/10.1016/1359-0189(90)90036-W, 1990.

Gerardin, M., Milesi, G., Mercadier, J., Cathelineau, M., and Bartier, D.: Development of an integrated analytical platform for clay mineral separation, characterization and K–Ar dating, Geosci. Instrum. Method. Data Syst., 13, 309–323, https://doi.org/10.5194/gi-13-309-2024, 2024.

Glodny, J. and Grauert, B.: Evolution of a hydrothermal fluid-rock interaction system as recorded by Sr isotopes: A case study from the Schwarzwald, SW Germany, Miner. Petrol., 95, 163–178, https://doi.org/10.1007/s00710-008-0034-1, 2009.

Glodek, M., Schels, M., and Schwenker, F.: Ensemble Gaussian mixture models for probability density estimation, Comput. Stat., 28, 127–138, https://doi.org/10.1007/s00180-012-0374-5, 2013.

Glorie, S., Gilbert, S. E., Hand, M., and Lloyd, J. C.: Calibration methods for laser ablation Rb–Sr geochronology: comparisons and recommendation based on NIST glass and natural reference materials, Geochronology, 6, 21–36, https://doi.org/10.5194/gchron-6-21-2024, 2024.

Grand'Homme, A., Janots, E., Bosse, V., Seydoux-Guillaume, A. M., and De Ascenção Guedes, R.: Interpretation of U-Th-Pb in-situ ages of hydrothermal monazite-(Ce) and xenotime-(Y): evidence from a large-scale regional study in clefts from the western alps, Miner. Petrol., 110, 787–807, https://doi.org/10.1007/s00710-016-0451-5, 2016.

Gyomlai, T., Agard, P., Herviou, C., Jolivet, L., Monié, P., Mendes, K., and Iemmolo, A.: In situ Rb–Sr and 40Ar-39Ar dating of distinct mica generations in the exhumed subduction complex of the Western Alps, Contrib. Mineral. Petrol., 178, 58, https://doi.org/10.1007/s00410-023-02042-8, 2023.

Halter, G.: Zonalite des alterations dans l'environnement des gisements d'uranium associes a la discordance du proterozoique moyen (saskatchewan, canada), These de doctorat, Univer-

sité Louis Pasteur (Strasbourg), 1971–2008, https://theses.fr/1988STR13078 (last access: 3 July 2026), 1988.

Hastie, T., Friedman, J., and Tibshirani, R.: The Elements of Statistical Learning, Springer New York, New York, NY, https://doi.org/10.1007/978-0-387-21606-5, 2001.

Hobson, G. D., Geological Survey of Canada, and MacAulay, H. A.: A Seismic Reconnaissance Survey of the Athabasca Formation, Alberta and Saskatchewan (part of 74), Department of Energy, Mines and Resources, 36 pp., https://publications.gc.ca/collections/collection_2016/rncan-nrcan/M44-69-18-eng.pdf (last access: 6 July 2026), 1969.

Hoeve, J. and Sibbald, T. I. I.: On the genesis of Rabbit Lake and other unconformity-type uranium deposits in northern Saskatchewan, Canada, Econ. Geol., 73, 1450–1473, https://doi.org/10.2113/gsecongeo.73.8.1450, 1978.

Hogmalm, K. J., Zack, T., Karlsson, A. K.-O., Sjöqvist, A. S. L., and Garbe-Schönberg, D.: In situ Rb–Sr and K-Ca dating by LA-ICP-MS/MS: an evaluation of N_2O and SF_6 as reaction gases, J. Anal. Atom. Spectrom., 32, 305–313, https://doi.org/10.1039/C6JA00362A, 2017.

Holness, M.: PARNELL, J. (Ed.): Dating and Duration of Fluid Flow and Fluid-Rock Interaction. Geological Society Special Publication no. 144. vi+284 pp., ISBN 1 86239 019 3, Geological Magazine, 137, 705–712, https://doi.org/10.1017/S0016756800274736, 2000.

Huang, C., Wang, H., Xie, L., Xu, L., Wu, S., Yang, Y., and Yang, J.: High-precision Rb–Sr isotope analysis with Neoma MS/MS: Enhancing in situ geochronology by laser ablation, Spectrochim. Acta Part B, 224, 107117, https://doi.org/10.1016/j.sab.2025.107117, 2025.

Huang, Y., Qi, X., Wu, Q., Li, J., Ren, M., Duan, L., Xiong, T., Yang, Z., Zhao, Y., Ciren, L., Wei, W., Duan, J., and Yan, M.: In Situ Rb-Sr Dates of Muscovite and Sulfur Isotope of Pyrite from the Yangshan Gold Deposit in Western Qinling, China, Acta Geol. Sin.-Engl., 97, 1475–1489, https://doi.org/10.1111/1755-6724.15091, 2023.

Hueck, M., Wemmer, K., Ksienzyk, A. K., Kuehn, R., and Vogel, N.: Potential, premises, and pitfalls of interpreting illite argon dates – A case study from the German Variscides, Earth-Sci. Rev., 232, 104133, https://doi.org/10.1016/j.earscirev.2022.104133, 2022.

Jeanneret, P., Goncalves, P., Durand, C., Trap, P., Marquer, D., Quirt, D., and Ledru, P.: Tectono-metamorphic evolution of the pre-Athabasca basement within the Wollaston–Mudjatik Transition Zone, Saskatchewan, Can. J. Earth Sci., 53, 231–259, https://doi.org/10.1139/cjes-2015-0136, 2016.

Jeanneret, P., Goncalves, P., Durand, C., Poujol, M., Trap, P., Marquer, D., Quirt, D., and Ledru, P.: Geochronological constraints on the trans-Hudsonian tectono-metamorphic evolution of the pre-Athabasca basement within the Wollaston-Mudjatik Transition Zone, Saskatchewan, Precambrian Res., 301, 152–178, https://doi.org/10.1016/j.precamres.2017.07.019, 2017.

Jefferson, C. W., Thomas, D. J., Gandhi, S. S., Ramaekers, P., Delaney, G., Brisbin, D., Cutts, C., Portella, P., and Olson, R. A.: Unconformity-associated uranium deposits of the Athabasca Basin, Saskatchewan and Alberta, Geological Survey of Canada, Bulletin 588, 23–67, https://doi.org/10.4095/223744, 2007.

Jegal, Y., Zimmermann, C., Reisberg, L., Yeghicheyan, D., Cloquet, C., Peiffert, C., Gerardin, M., Deloule, E., and Mercadier, J.: Characterisation of Reference Materials for In Situ Rb-Sr Dating by LA-ICP-MS/MS, Geostandard Geoanalytic Res., 46, 645–671, https://doi.org/10.1111/ggr.12456, 2022.

Jenkin, G. R. T., Ellam, R. M., Rogers, G., and Stuart, F. M.: An investigation of closure temperature of the biotite Rb–Sr system: The importance of cation exchange, Geochim. Cosmochim. Ac., 65, 1141–1160, https://doi.org/10.1016/S0016-7037(00)00560-3, 2001.

Juhász, A., Tóth, T. M., Ramseyer, K., and Matter, A.: Connected fluid evolution in fractured crystalline basement and overlying sediments, Pannonian Basin, SE Hungary, Chem. Geol., 182, 91–120, https://doi.org/10.1016/S0009-2541(01)00269-8, 2002.

Kaczowka, A. J., Kyser, T. K., Kotzer, T. G., Leybourne, M. I., and Layton-Matthews, D.: Geometallurgical ore characterization of the high-grade polymetallic unconformity-related uranium deposit, Can. Mineral., 59, 813–845, https://doi.org/10.3749/canmin.2000050, 2021.

Kalt, A., Grauert, B., and Baumann, A.: Rb-Sr and U-Pb isotope studies on migmatites from the Schwarzwald (Germany): constraints on isotopic resetting during Variscan high-temperature metamorphism, J. Metamorph. Geol., 12, 667–680, https://doi.org/10.1111/j.1525-1314.1994.tb00050.x, 1994.

Karlstrom, K. E. and Bowring, S. A.: Early Proterozoic Assembly of Tectonostratigraphic Terranes in Southwestern North America, J. Geol., 96, 561–576, 1988.

Kister, P.: Mobilité des éléments géochimiques dans un bassin sédimentaire clastique, du Protérozoïque à nos jours: le bassin Athabasca (Saskatchewan, Canada), PhD thesis, Institut National Polytechnique de Lorraine, https://theses.fr/2003INPL062N (last access: 3 July 2026), 2003.

Kister, P., Vieillard, P., Cuney, M., Quirt, D., and Laverret, E.: Thermodynamic constraints on the mineralogical and fluid composition evolution in a clastic sedimentary basin: the Athabasca Basin (Saskatchewan, Canada), Eur. J. Mineral., 17, 325–341, https://doi.org/10.1127/0935-1221/2005/0017-0325, 2005.

Kohn, M.: Titanite Petrochronology, Reviews in Mineralogy and Geochemistry, 83, 419–441, https://doi.org/10.2138/rmg.2017.83.13, 2017

Kotzer, T. G. and Kyser, T. K.: Fluid history of the Athabasca Basin and its relation to uranium deposits. Saskatchewan Energy and Mines, Saskatchewan Geological Survey Miscellaneous Report, 90, 153–157, 1990.

Kotzer, T. G. and Kyser, T. K.: Petrogenesis of the Proterozoic Athabasca Basin, northern Saskatchewan, Canada, and its relation to diagenesis, hydrothermal uranium mineralization and paleohydrogeology, Chem. Geol., 120, 45–89, https://doi.org/10.1016/0009-2541(94)00114-N, 1995.

Kyser, K., Hiatt, E., Renac, C., Durocher, K., Holk, G., and Deckart, K.: Diagenetic fluids in Paleo-and Meso-Proterozoic sedimentary basins and their implications for long protracted fluid histories, Mineralogical Association of Canada Short Course, 28, 225–262, 2000.

Kyser, K., Lahusen, L., Drever, G., Dunn, C., Leduc, E., and Chipley, D.: Using Pb isotopes in surface media to distinguish anthropogenic sources from undercover uranium sources, CR. Géosci., 347, 215–226, 2015.

Liebmann, J., Kirkland, C. L., Kelsey, D. E., Korhonen, F. J., and Rankenburg, K.: Lithological fabric as a proxy

for Rb–Sr isotopic complexity, Chem. Geol., 608, 121041, https://doi.org/10.1016/j.chemgeo.2022.121041, 2022.

Liu, W., Zhang, X., Zhang, J., and Jiang, M.: Sphalerite Rb–Sr Dating and in situ Sulfur Isotope Analysis of the Daliangzi Lead-Zinc Deposit in Sichuan Province, SW China, J. Earth Sci., 29, 573–586, https://doi.org/10.1007/s12583-018-0785-5, 2018.

Macdonald, C. C.: Mineralogy and geochemistry of a Precambrian regolith in the Athabasca Basin, M.Sc. thesis, University of Saskatchewan, Saskatoon, 151 pp., https://harvest.usask.ca/items/624e4ca2-79ed-4992-96a1-43b560a60e4d (last access: 6 July 2026), 1980.

Mao, G., Hua, R., Long, G., and Lu, H.: Rb-Sr Dating of Pyrite and Quartz Fluid Inclusions and Origin of Ore-forming Materials of the Jinshan Gold Deposit, Northeast Jiangxi Province, South China, Ac. Geol. Sin.-Engl., 87, 1658–1667, https://doi.org/10.1111/1755-6724.12166, 2013.

McLachlan, G. and Peel, D.: Finite Mixture Models, 1st edn., Wiley, https://doi.org/10.1002/0471721182, 2000.

Martz, P.: Caractéristiques, chronologie et rôles des circulations fluides dans le bassin d'Athabasca et son socle: implications dans la formation et l'évolution du gisement d'uranium de Cigar Lake, Thèse de doctorat, Université de Lorraine, https://theses.hal.science/tel-01816179v2/file/DDOC_T_2017_0221_MARTZ.pdf (last access: 6 July 2026), 2017.

Martz, P., Mercadier, J., Cathelineau, M., Boiron, M.-C., Quirt, D., Doney, A., Gerbeaud, O., De Wally, E., and Ledru, P.: Formation of U-rich mineralizing fluids through basinal brine migration within basement-hosted shear zones: A large-scale study of the fluid chemistry around the unconformity-related Cigar Lake U deposit (Saskatchewan, Canada), Chem. Geol., 508, 116–143, https://doi.org/10.1016/j.chemgeo.2018.05.042, 2019a.

Matheney, R. K., Brookins, D. G., Wallin, E. T., Shafiqullah, M., and Damon, P. E.: Incompletely reset Rb–Sr systems from a Cambrian red-rock granophyre terrane, Florida Mountains, New Mexico, USA, Chem. Geol.: Isotope Geoscience section, 86, 29–47, https://doi.org/10.1016/0168-9622(90)90004-V, 1990.

Melnykov, V. and Melnykov, I.: Initializing the EM algorithm in Gaussian mixture models with an unknown number of components, Comput. Stat. Data An., 56, 1381–1395, https://doi.org/10.1016/j.csda.2011.11.002, 2012.

McFarlane, C. R. M. and Harrison, T. M.: Pb-diffusion in monazite: Constraints from a high-T contact aureole setting, Earth Planet. Sc. Lett., 250, 376–384, https://doi.org/10.1016/j.epsl.2006.06.050, 2006.

McGill, B. D., Marlat, J. L., Matthews, R. B., Sopuck, V. J., Homeniuk, L. A., and Hubregtse, J. J.: The P2 North uranium deposit, Saskatchewan, Canada, Explor. Min. Geol., 2, 321–331, 1993.

McLachlan, G. J., Lee, S. X., and Rathnayake, S. I.: Finite Mixture Models, Annu. Rev. Stat. Appl., 6, 355–378, https://doi.org/10.1146/annurev-statistics-031017-100325, 2019.

Menier, A., Roy, R., Harrison, G., Zerff, R. W., and Kinar, D.: Relationship between rock physical properties and spectral mineralogy applied to exploration for an unconformity-related uranium deposit (Saskatchewan, Canada), Can. J. Earth Sci., 57, 1349–1364, https://doi.org/10.1139/cjes-2019-0080, 2020.

Mercadier, J., Cuney, M., Cathelineau, M., and Lacorde, M.: U redox fronts and kaolinisation in basement-hosted unconformity-related U ores of the Athabasca Basin (Canada): late U remobilisation by meteoric fluids, Miner. Deposita, 46, 105–135, https://doi.org/10.1007/s00126-010-0314-7, 2011.

Mercadier, J., Richard, A., and Cathelineau, M.: Boron- and magnesium-rich marine brines at the origin of giant unconformity-related uranium deposits: δ^{11}B evidence from Mg-tourmalines, Geology, 40, 231–234, https://doi.org/10.1130/G32509.1, 2012.

Młynarska, M., Barnes, C. J., Zack, T., Majka, J., and Mazur, S.: In situ white mica Rb / Sr geochronology of the Leszczyniec metaigneous complex, West Sudetes: evidence of upper plate deformation at the onset of Variscan collision, Int. J. Earth Sci.-Geol. Rundsch., 113, 319–333, https://doi.org/10.1007/s00531-023-02373-8, 2024.

Muñoz-Montecinos, J., Giuliani, A., Oesch, S., Volante, S., Peters, B., and Behr, W.: In situ rubidium–strontium geochronology of white mica in young metamafic and metasomatic rocks from Syros: testing the limits of laser-ablation triple-quadrupole inductively coupled plasma mass spectrometer mica dating using different anchoring approaches, Geochronology, 6, 585–605, https://doi.org/10.5194/gchron-6-585-2024, 2024.

Ng, R., Alexandre, P., Kyser, K., Cloutier, J., Abdu, Y. A., and Hawthorne, F. C.: Oxidation state of iron in alteration minerals associated with sandstone-hosted unconformity-related uranium deposits and apparently barren alteration systems in the Athabasca Basin, Canada: Implications for exploration, J. Geochem. Explor., 130, 22–43, https://doi.org/10.1016/j.gexplo.2013.02.009, 2013.

Nguyen, H. and McLachlan, G.: Maximum likelihood estimation of Gaussian mixture models without matrix operations, Adv. Data Anal. Classi., 9, https://doi.org/10.1007/s11634-015-0209-7, 2015.

Obin, T.: Mobilités du carbone et du soufre dans l'environnement du Bassin de l'Athabasca (Saskatchewan, Canada) et impact(s) sur la formation des gisements d'uranium de type discordance, Thèse de doctorat, Université de Lorraine, https://theses.fr/2025LORR0092 (last access: 6 July 2026), 2025.

Olierook, H. K. H., Rankenburg, K., Ulrich, S., Kirkland, C. L., Evans, N. J., Brown, S., McInnes, B. I. A., Prent, A., Gillespie, J., McDonald, B., and Darragh, M.: Resolving multiple geological events using in situ Rb–Sr geochronology: implications for metallogenesis at Tropicana, Western Australia, Geochronology, 2, 283–303, https://doi.org/10.5194/gchron-2-283-2020, 2020.

Oummouch, A., Essaifi, A., Zayane, R., Maddi, O., Zouhair, M., and Maacha, L.: Geology and Metallogenesis of the Sediment-Hosted Cu-Ag Deposit of Tizert (Igherm Inlier, Anti-Atlas Copperbelt, Morocco), Geofluids, 2017, 7508484, https://doi.org/10.1155/2017/7508484, 2017.

Pacquet, A. and Weber, F.: Pétrographie et minéralogie des halos d'altération autour du gisement de Cigar Lake et leurs relations avec les minéralisations, Can. J. Earth Sci., 30, 674–688, https://doi.org/10.1139/e93-055, 1993.

Pagel, M.: Cadre géologique des gisements d'uranium dans la structure de Carswell (Saskatchewan, Canada). Etudes des phases fluides, Thèse de 3ème cycle, Université de Nancy, Nancy, France, 1975a.

Pagel, M.: Détermination des conditions physico-chimiques de la silicification diagénétique des grès Athabasca (Canada) au moyen des inclusions fluides, Comptes Rendus Académie Sci. Paris, Série D, 280, 2301–2304, 1975b.

Paton, C., Hellstrom, J., Paul, B., Woodhead, J., and Hergt, J.: Iolite: Freeware for the visualisation and processing of mass spectrometric data, J. Anal. Atom. Spectrom., 26, 2508–2518, https://doi.org/10.1039/C1JA10172B, 2011.

Pehrsson, S., Eglington, B., Rainbird, R., Regis, D., Ramaekers, P., and Jefferson, C.: Extent and significance of the Racklan-Forward Orogen in Canada: far-field interior reactivation during Nuna assembly, Geological Society, London, Special Publications, 531, 47–75, https://doi.org/10.1144/SP531-2022-307, 2023.

Percival, J. B. and Kodama, H.: Sudoite from cigar lake, Saskatchewan, Can. Mineral., 27, 633–641, 1989.

Philippe, S., Lancelot, J. R., Clauer, N., and Pacquet, A.: Formation and evolution of the Cigar Lake uranium deposit based on U–Pb and K–Ar isotope systematics, Can. J. Earth Sci., 30, 720–730, https://doi.org/10.1139/e93-058, 1993.

Powell, J. W., Percival, J. B., Potter, E. G., Van Der Lelij, R., and Xie, R.: Mineralogy and K–Ar geochronology of clay alteration associated with uranium mineralization in the Patterson Lake Corridor, Saskatchewan, Geochem.: Explor. Environ. Anal., 22, geochem2021-061, https://doi.org/10.1144/geochem2021-061, 2022.

Qiu, E., Larson, K. P., Camacho, A., and Zhang, Y.: Reassessing the timing of high-strain deformation in the Strangways Metamorphic Complex, Central Australia, by in situ mica Rb–Sr and titanite U–Pb geochronology, J. Geol. Soc., 181, jgs2023-163, https://doi.org/10.1144/jgs2023-163, 2024.

Rabiei, M., Chi, G., Normand, C., Davis, W. J., Fayek, M., and Blamey, N. J. F.: Hydrothermal Rare Earth Element (Xenotime) Mineralization at Maw Zone, Athabasca Basin, Canada, and Its Relationship to Unconformity-Related Uranium Deposits, Econ. Geol., 112, 1483–1507, https://doi.org/10.5382/econgeo.2017.4518, 2017.

Rainbird, R. H., Stern, R. A., Rayner, N., Jefferson, C. W., and Delaney, G.: Age, provenance, and regional correlation of the Athabasca Group, Saskatchewan and Alberta, constrained by igneous and detrital zircon geochronology, Bulletin-Geological Survey of Canada, 588, 193, https://www.researchgate.net/publication/292432047_Age_provenance_and_regional_correlation_of_the_Athabasca_Group_Saskatchewan_and_Alberta_constrained_by_igneous_and_detrital_zircon_geochronology_EXTECH_IV_Geology_and_Uranium_EXploration_TECHnology_of (last access: 3 July 2026), 2007.

Ramaekers, P., Jefferson, C. W., Yeo, G. M., Collier, B., Long, D. G. F., Drever, G., McHardy, S., Jiricka, D., Cutts, C., and Wheatley, K.: Revised geological map and stratigraphy of the Athabasca Group, Saskatchewan and Alberta, Bulletin-Geological Survey of Canada, 588, 155, https://www.researchgate.net/publication/279571432_Revised_geological_map_and_stratigraphy_of_the_Athabasca_group_Saskatchewan_and_Alberta (last access: 3 July 2026), 2007.

Rasmussen, B., Fletcher, I. R., and McNaughton, N. J.: Dating low-grade metamorphic events by SHRIMP U–Pb analysis of monazite in shales, Geology, https://doi.org/10.1130/0091-7613(2001)029<0963:DLGMEB>2.0.CO;2, 29, 963, 2001.

Rasmussen, B., Sheppard, S., and Fletcher, I. R.: Testing ore deposit models using in situ U–Pb geochronology of hydrothermal monazite: Paleoproterozoic gold mineralization in northern Australia, Geology, 34, 77–80, https://doi.org/10.1130/G22058.1, 2006.

Rasmussen, B., Zi, J.-W., and Muhling, J. R.: Tectonic fluid expulsion: U–Pb evidence for punctuated hydrothermal fluid flow and hydraulic fracturing during orogenesis, Earth Planet. Sc. Lett., 604, 117997, https://doi.org/10.1016/j.epsl.2023.117997, 2023.

Redaa, A., Farkaš, J., Gilbert, S., Collins, A. S., Wade, B., Löhr, S., Zack, T., and Garbe-Schönberg, D.: Assessment of elemental fractionation and matrix effects during in situ Rb–Sr dating of phlogopite by LA-ICP-MS/MS: implications for the accuracy and precision of mineral ages, J. Anal. Atom. Spectrom., 36, 322–344, https://doi.org/10.1039/D0JA00299B, 2021.

Redaa, A., Farkaš, J., Hassan, A., Collins, A. S., Gilbert, S., and Löhr, S. C.: Constraints from in-situ Rb–Sr dating on the timing of tectono-thermal events in the Umm Farwah shear zone and associated Cu-Au mineralisation in the Southern Arabian Shield, Saudi Arabia, J. Asian Earth Sci., 224, 105037, https://doi.org/10.1016/j.jseaes.2021.105037, 2022.

Reynolds, R. C. and Thomson, C. H.: Illite from the Potsdam Sandstone of New York: A Probable Noncentrosymmetric Mica Structure, Clay. Clay Miner., 41, 66–72, https://doi.org/10.1346/CCMN.1993.0410107, 1993.

Ribeiro, B. V., Kirkland, C. L., Finch, M. A., Faleiros, F. M., Reddy, S. M., Rickard, W. D. A., and Hartnady, M. I. H.: Microstructures, geochemistry, and geochronology of mica fish: Review and advances, J. Struct. Geol., 175, 104947, https://doi.org/10.1016/j.jsg.2023.104947, 2023a.

Ribeiro, B. V., Kirkland, C. L., Kelsey, D. E., Reddy, S. M., Hartnady, M. I. H., Faleiros, F. M., Rankenburg, K., Liebmann, J., Korhonen, F. J., and Clark, C.: Time-strain evolution of shear zones from petrographically constrained Rb–Sr muscovite analysis, Earth Planet. Sc. Lett., 602, 117969, https://doi.org/10.1016/j.epsl.2022.117969, 2023b.

Richard, A., Banks, D. A., Mercadier, J., Boiron, M.-C., Cuney, M., and Cathelineau, M.: An evaporated seawater origin for the ore-forming brines in unconformity-related uranium deposits (Athabasca Basin, Canada): Cl/Br and δ^{37}Cl analysis of fluid inclusions, Geochim. Cosmochim. Ac., 75, 2792–2810, https://doi.org/10.1016/j.gca.2011.02.026, 2011.

Richard, A., Cauzid, J., Cathelineau, M., Boiron, M.-C., Mercadier, J., and Cuney, M.: Synchrotron XRF and XANES investigation of uranium speciation and element distribution in fluid inclusions from unconformity-related uranium deposits, Geofluids, 13, 101–111, https://doi.org/10.1111/gfl.12009, 2013.

Richard, A., Montel, J.-M., Leborgne, R., Peiffert, C., Cuney, M., and Cathelineau, M.: Monazite Alteration in $H_2O \pm HCl \pm NaCl \pm CaCl_2$ Fluids at 150 °C and psat: Implications for Uranium Deposits, Minerals, 5, 693–706, https://doi.org/10.3390/min5040518, 2015.

Rösel, D. and Zack, T.: LA-ICP-MS/MS Single-Spot Rb-Sr Dating, Geostandard Geoanalytic Res., 46, 143–168, https://doi.org/10.1111/ggr.12414, 2022.

Saito, T., Qiu, H.-N., Shibuya, T., Li, Y.-B., Kitajima, K., Yamamoto, S., Ueda, H., Komiya, T., and Maruyama, S.: Ar–Ar dating for hydrothermal quartz from the 2.4 Ga Ongeluk Formation, South Africa: implications for seafloor hydrothermal circulation, R Soc Open Sci, 5, 180260, https://doi.org/10.1098/rsos.180260, 2018.

Schneider, D. A., Heizler, M. T., Bickford, M. E., Wortman, G. L., Condie, K. C., and Perilli, S.: Timing constraints of orogeny to cratonization: Thermochronology of the Paleoproterozoic Trans-Hudson orogen, Manitoba and Saskatchewan, Canada, Precambrian Res., 153, 65–95, https://doi.org/10.1016/j.precamres.2006.11.007, 2007.

Scott Anderson, F., Levine, J., and Whitaker, T. J.: Rb–Sr resonance ionization geochronology of the Duluth Gabbro: A proof of concept for in situ dating on the Moon, Rapid Commun. Mass Sp., 29, 1457–1464, https://doi.org/10.1002/rcm.7253, 2015.

Şengün, F., Bertrandsson Erlandsson, V., Hogmalm, J., and Zack, T.: In situ Rb–Sr dating of K-bearing minerals from the orogenic Akçaabat gold deposit in the Menderes Massif, Western Anatolia, Turkey, J. Asian Earth Sci., 185, 104048, https://doi.org/10.1016/j.jseaes.2019.104048, 2019.

Schmitz, B., Biermanns, P., Hueck, M., Wemmer, K., Schmid, S. M., Onuzi, K., Reicherter, K., and Ustaszewski, K.: Kinematics and Age of the Orogen-Perpendicular Shkoder-Peja Normal Fault in North Albania Constrained by Fault-Slip Data, Raman Spectroscopy and K–Ar Fault-Gouge Dating, Tectonics, American Geophysical Union, 44, e2024TC008660, https://doi.org/10.1029/2024TC008660, 2025.

Sibson, R. H.: Conditions for fault-valve behaviour, Geological Society, London, Special Publications, 54, 15–28, https://doi.org/10.1144/GSL.SP.1990.054.01.02, 1990.

Sims, P. K. and Peterman, Z. E.: Early Proterozoic Central Plains orogen: A major buried structure in the north-central United States, Geology, 14, 488–491, 1986.

Skipton, D. R., St-Onge, M. R., Schneider, D. A., and McFarlane, C. R. M.: Tectonothermal Evolution of the Middle Crust in the Trans-Hudson Orogen, Baffin Island, Canada: Evidence from Petrology and Monazite Geochronology of Sillimanite-bearing Migmatites, J. Petrol., 57, 1437–1462, https://doi.org/10.1093/petrology/egw046, 2016.

Skirrow, R. G., Mercadier, J., Armstrong, R., Kuske, T., and Deloule, E.: The Ranger uranium deposit, northern Australia: Timing constraints, regional and ore-related alteration, and genetic implications for unconformity-related mineralisation, Ore Geol. Rev., 76, 463–503, https://doi.org/10.1016/j.oregeorev.2015.09.001, 2016.

Sundvoll, B. and Larsen, B. T.: Rb–Sr isotope systematics in the magmatic rocks of the Oslo Rift, Norges Geologiske Undersøkelse, Bulletin 418, 27–46, https://www.semanticscholar.org/paper/Rb-Sr-isotope-systematics (last access: 3 July 2026), 1990.

Tian, J., Wang, J., Tian, T., Wang, L., Wang, Y., Yu, X., Zhang, W., Ren, T., and Sun, B.: In-Situ Geochemical and Rb–Sr Dating Analysis of Sulfides from a Gold Deposit Offshore of Northern Sanshandao, Jiaodong Peninsula, North China: Implications for Gold Mineralization, Minerals, 14, 456, https://doi.org/10.3390/min14050456, 2024.

Tichomirowa, M., Käßner, A., Sperner, B., Lapp, M., Leonhardt, D., Linnemann, U., Münker, C., Ovtcharova, M., Pfänder, J. A., Schaltegger, U., Sergeev, S., von Quadt, A., and Whitehouse, M.: Dating multiply overprinted granites: The effect of protracted magmatism and fluid flow on dating systems (zircon U–Pb: SHRIMP/SIMS, LA-ICP-MS, CA-IDTIMS; and Rb–Sr, Ar–Ar) – Granites from the Western Erzgebirge (Bohemian Massif, Germany), Chem. Geol., 519, 11–38, https://doi.org/10.1016/j.chemgeo.2019.04.024, 2019.

Tran, H., Ansdell, K., Bethune, K., Ashton, K., and Hamilton, M.: Provenance and tectonic setting of Paleoproterozoic metasedimentary rocks along the eastern margin of Hearne craton: Constraints from SHRIMP geochronology, Wollaston Group, Saskatchewan, Canada, Precambrian Res., 167, 171–185, https://doi.org/10.1016/j.precamres.2008.08.003, 2008.

Toma, J., Creaser, R. A., Card, C., Stern, R. A., Chacko, T., and Steele-MacInnis, M.: Re-Os systematics and chronology of graphite, Geochim. Cosmochim. Ac., 323, 164–182, https://doi.org/10.1016/j.gca.2022.02.012, 2022.

Toma, J., Creaser, R. A., Card, C., Pana, D., Dufrane, A., and Li, L.: Nuna supercontinent assembly linked to carbon cycling in shear zones 1.9–1.7 billion years ago, Nat. Geosci., 17, 1038–1045, https://doi.org/10.1038/s41561-024-01519-w, 2024.

Velde, B. and Christophe, R.: Smectite to illite conversion and K–AR ages, Clay Miner., 31, 25–32, 1996.

Vermeesch, P.: IsoplotR: A free and open toolbox for geochronology, Geosci. Front., 9, 1479–1493, https://doi.org/10.1016/j.gsf.2018.04.001, 2018.

Villa, I. M.: Isotopic closure, Terra Nova, 10, 42–47, https://doi.org/10.1046/j.1365-3121.1998.00156.x, 1998.

Villa, I. M.: Dating deformation: the role of atomic-scale processes, J. Geol. Soc., 179, jgs2021-098, https://doi.org/10.1144/jgs2021-098, 2022.

Viswanathan, H. S., Ajo-Franklin, J., Birkholzer, J. T., Carey, J. W., Guglielmi, Y., Hyman, J. D., Karra, S., Pyrak-Nolte, L. J., Rajaram, H., Srinivasan, G., and Tartakovsky, D. M.: From Fluid Flow to Coupled Processes in Fractured Rock: Recent Advances and New Frontiers, Rev. Geophys., 60, e2021RG000744, https://doi.org/10.1029/2021RG000744, 2022.

Walawender, M. J., Gastil, R. G., Clinkenbeard, J. P., McCormick, W. V., Eastman, B. G., Wernicke, R. S., Wardlaw, M. S., Gunn, S. H., and Smith, B. M.: Chapter 1: Origin and evolution of the zoned La Posta-type plutons, eastern Peninsular Ranges batholith, southern and Baja California, in: Geological Society of America Memoirs, vol. 174, Geological Society of America, 1–18, https://doi.org/10.1130/MEM174-p1, 1990.

Walter, B., Géraud, Y., Bartier, D., Kluska, J.-M., Diraison, M., Morlot, C., and Raisson, F.: Petrophysical and mineralogical evolution of weathered crystalline basement in western Uganda: Implications for fluid transfer and storage, AAPG Bulletin, 102, 1035–1065, https://doi.org/10.1306/0810171610917171, 2018.

Wang, C., Alard, O., Lai, Y.-J., Foley, S. F., Liu, Y., Munnikhuis, J., and Wang, Y.: Advances in in-situ Rb–Sr dating using LA-ICP-MS/MS: applications to igneous rocks of all ages and to the identification of unrecognized metamorphic events, Chem. Geol., 610, 121073, https://doi.org/10.1016/j.chemgeo.2022.121073, 2022.

Weinberg, R. F., Wolfram, L. C., Nebel, O., Hasalová, P., Závada, P., Kylander-Clark, A. R. C., and Becchio, R.: Decoupled U–Pb date and chemical zonation of monazite in migmatites: The case for disturbance of isotope systematics by coupled dissolution-reprecipitation, Geochim. Cosmochim. Ac., 269, 398–412, https://doi.org/10.1016/j.gca.2019.10.024, 2020.

Willigers, B. J. A., Mezger, K., and Baker, J. A.: Development of high precision Rb–Sr phlogopite and biotite geochronology; an alternative to $^{40}Ar/^{39}Ar$ tri-

octahedral mica dating, Chem. Geol., 213, 339–358, https://doi.org/10.1016/j.chemgeo.2004.07.006, 2004.

Woodhead, J. D. and Hergt, J. M.: Strontium, Neodymium and Lead Isotope Analyses of NIST Glass Certified Reference Materials: SRM 610, 612, 614, Geostandard. Newslett., 25, 261–266, https://doi.org/10.1111/j.1751-908X.2001.tb00601.x, 2001.

Worden, J. M., Cumming, G. L., and Baadsgaard, H.: Geochronology of host rocks and mineralization of the Midwest uranium deposit, northern Saskatchewan, edited by: Sibbald, T. I. and Petruk, W., Geology of Uranium Deposits, CIM An. Conf., 32, 67–72, 1985.

Yardley, B. W. D.: Quartz veins and devolatilization during metamorphism, J. Geol. Soc., 140, 657-663, https://doi.org/10.1144/gsjgs.140.4.0657, 1983.

Yardley, B. W. D. and Bodnar, R. J.: Fluids in the Continental Crust, GeochemPersp, 3, 1–127, https://doi.org/10.7185/geochempersp.3.1, 2014.

Yeo, G. M. and Delaney, G.: The Wollaston Supergroup, stratigraphy and metallogeny of a Paleoproterozoic Wilson cycle in the Trans-Hudson Orogen, Saskatchewan, Geological Survey of Canada, Bulletin 588, 89–117, https://doi.org/10.4095/223746, 2007.

Zack, T. and Hogmalm, K. J.: Laser ablation Rb / Sr dating by online chemical separation of Rb and Sr in an oxygen-filled reaction cell, Chem. Geol., 437, 120–133, https://doi.org/10.1016/j.chemgeo.2016.05.027, 2016.

Zametzer, A., Kirkland, C. L., Barham, M., Hartnady, M. I. H., Bath, A. B., and Rankenburg, K.: Episodic alteration within a gold-bearing Archean shear zone revealed by in situ biotite Rb–Sr dating, Precambrian Res., 382, 106872, https://doi.org/10.1016/j.precamres.2022.106872, 2022.